

# Testing Mantle Convection Simulations with Paleobiology and Other Stratigraphic Observations: Examples from Western North America

Victoria M. Fernandes<sup>1,2</sup>, Gareth G. Roberts<sup>2</sup>, Fred Richards<sup>2</sup>

<sup>1</sup>GFZ Potsdam, Helmholtz Zentrum, Telegrafenberg, 14473 Potsdam, Germany

<sup>2</sup>Department of Earth Science and Engineering, Imperial College London, South Kensington Campus, SW7 2AZ, UK.

## Key Points:

- Large-scale digital inventories of stratigraphic observations used to test predictions from mantle convection simulations.
  - Useful diagnostics include net uplift and subsidence, absolute elevations, paleo-water depths.
  - Upper mantle thermo-mechanical evolution—crucial for assessing sub-plate support—constrained using stratigraphy.

13 **Abstract**

14 Mantle convection plays a fundamental role in driving evolution of oceanic and continental litho-  
 15 sphere. In turn it impacts a broad suite of processes operating at or close to Earth's surface includ-  
 16 ing landscape evolution, glacio-eustasy, magmatism and climate. A variety of theoretical approaches  
 17 now exist to simulate mantle convection. Outputs from such simulations are being used to param-  
 18 eterise models of landscape evolution and basin formation. However, the substantial body of exist-  
 19 ing simulations has generated a variety of conflicting views on the history of dynamic topography,  
 20 its evolution and key parameters for modeling mantle flow. The focus of this study is on develop-  
 21 ing strategies to use large-scale quantitative stratigraphic observations to assess model predictions  
 22 and identify simulation parameters that generate realistic predictions of Earth surface evolution. Spot  
 23 measurements of uplift or subsidence provide useful target observations for models of dynamic to-  
 24 polography, but finding areas where tectonics have not also influenced vertical motions is challeng-  
 25 ing. To address this issue, we use large inventories of stratigraphic data from across North Amer-  
 26 ica with contextual geophysical and geodetic data to constrain the regional uplift and subsidence  
 27 history. We demonstrate that a suite of typical geodynamic simulations struggle to match the am-  
 28 plitude, polarity and timing of observed vertical motions. Building on recent seismological advances,  
 29 we then explore strategies for understanding patterns of continental uplift and subsidence that in-  
 30 corporate (and test) predicted evolution of the lithosphere, asthenosphere and deep mantle. Our re-  
 31 sults demonstrate the importance of contributions from the uppermost mantle in driving vertical  
 32 motions of continental interiors.

33 **1 Introduction**

34    **1.1 Overview**

35 Mantle convection is generally accepted as an important driver of horizontal and vertical litho-  
 36 spheric motions (i.e., uplift and subsidence; *Pekeris*, 1935; *McKenzie & Jarvis*, 1980; *Parsons & Daly*,  
 37 1983; *Hager & Richards*, 1989; *Gurnis et al.*, 2000; *Hoggard et al.*, 2021). In turn, lithospheric motion  
 38 in response to mantle convection appears to play a key role in driving diverse geological, geo-  
 39 morphological, glacio-eustatic and climatic processes (e.g., *Austermann et al.*, 2015; *Salles et al.*,  
 40 2017; *Stephenson et al.*, 2019; *Richards et al.*, 2023). As such, there is considerable interest in de-  
 41 veloping reliable means to determine the history of mantle convection and its role in dictating the  
 42 history of Earth's surface. An important challenge is to produce or identify data of sufficient qual-  
 43 ity and spatio-temporal density to either directly constrain histories of mantle convection, or test  
 44 the fidelity of geodynamic simulations. In this contribution, we explore the use of substantial, dig-  
 45 ital, inventories of stratigraphic and paleobiological data to test vertical motion histories predicted  
 46 by models of mantle convection. In our view, stratigraphic observations are the least equivocal con-  
 47 straints on histories of lithospheric vertical motion available and provide a crucial test of geodynamic  
 48 simulations.

49 It is generally accepted that mantle convection is expressed in geological and geomorpholog-  
 50 ical processes including the generation of topography (e.g., *Parsons & Daly*, 1983; *Richards & Hager*,  
 51 1984; *Hager & Richards*, 1985), creation of accommodation space in sedimentary basins (e.g., *Lod-  
 52 hia et al.*, 2018; *Morris et al.*, 2020), changes in sea level (e.g., *Moucha et al.*, 2008), flooding of con-  
 53 tinental interiors and shoreline deformation and generation of stratigraphic hiatuses (e.g., *Rowley*  
 54 *et al.*, 2013; *Rovere et al.*, 2015; *Hayek et al.*, 2020,0; *Vilacís et al.*, 2022). It also appears to deter-  
 55 mine the planform and relief of continental drainage patterns (e.g., *Cox*, 1989; *Roberts et al.*, 2012;  
 56 *Czarnota et al.*, 2014; *Faccenna et al.*, 2019; *Lipp & Roberts*, 2021). In turn it likely impacts many  
 57 related phenomena operating at, or close to, Earth's surface, including climate (*Conway-Jones &*  
 58 *White*, 2022). Constraining amplitudes and histories of dynamic topography across scales of inter-  
 59 est is clearly crucial for understanding Earth's surface evolution. For mantle convection, these scales  
 60 include wavelengths,  $\lambda$ , set by the elastic strength of plates ( $O(10-10^2)$  km), to global scales (spher-  
 61 ical harmonic degree,  $l = 2$ ,  $\lambda = O(10^4)$  km; *Müller et al.*, 2018; *Ghelichkhan et al.*, 2021; *Holdt*  
 62 *et al.*, 2022). Methodologies to constrain sub-plate support sit in two broad categories.

First, geological, geophysical and geomorphological observations have been used to constrain modern and historic dynamic topography at specific localities (e.g., *Fernandes et al.*, 2019; *Morris et al.*, 2020; *Ball et al.*, 2021; *Holdt et al.*, 2022). The clearest observational guide to amplitudes, wavelengths and spectral power of modern dynamic topography arise from fitting spherical harmonic functions to oceanic age-depth measurements (e.g., *Hoggard et al.*, 2020; *Valentine & Davies*, 2020; *Holdt et al.*, 2022, strictly, models are fit to residuals from calibrated oceanic plate cooling histories).

The second suite of methodologies use geodynamic simulators to predict dynamic topography across the scales of interest (e.g., *McKenzie et al.*, 1974; *Hager & Richards*, 1989; *Gurnis*, 1988; *Bunge & Baumgardner*, 1995; *Flament et al.*, 2013; *Colli et al.*, 2016; *Müller et al.*, 2018; *Ghelichkhan et al.*, 2021). This approach, which now often makes use of geological (e.g., plate motion histories) and geophysical (e.g., seismic tomography) observations and theory to prescribe model properties (e.g., conversion of acoustic velocities into density; assimilation of tomographic models), provides means to explore theoretical responses and sensitivities of dynamic topography to calculated mantle evolution (e.g., *Flament et al.*, 2013; *Forte et al.*, 2009; *Liu et al.*, 2008; *Müller et al.*, 2018; *Faccenna et al.*, 2019; *Davies et al.*, 2023). There now exists a considerable body of mantle convection simulations, a few of which have been compared to independent geological observations at specific localities (e.g., New Jersey Margin, North America; *Flament et al.*, 2013) and to global power spectra of ocean age-depth residuals (*Hoggard et al.*, 2016). Model predictions, such as uplift and subsidence, have recently been coupled with models of lithospheric and landscape evolution to predict development of drainage networks and sedimentary basins (e.g., *Salles et al.*, 2017; *Faccenna et al.*, 2019; *Wang et al.*, 2020; *Ding et al.*, 2023).

Assessing sub-plate support of continents is generally more challenging than for oceans. The variability and complexity of continental lithosphere rheology, structure, and density complicate efforts to disentangle dynamic and isostatic contributions to topography (see, e.g., *Hoggard et al.*, 2021; *Stephenson et al.*, 2021). Nonetheless, assessing predictions, and changes, of continental sub-plate support has recently become considerably more tractable due to the improved availability of stratigraphic data (e.g., Macrostrat, Paleobiology Database). These data can be combined with geophysical observations (e.g., seismology; gravity anomalies) as well as other geological (e.g., magmatic) and geomorphological observations to constrain geometries and histories of sub-plate support (e.g., *Fernandes & Roberts*, 2021). As an example, in this paper we focus on Western North America, where stratigraphic data is dense and well documented. Additionally, a large body of magmatic and geophysical data is available to test predictions of mantle convection simulations. A considerable body of information regarding contextual tectonic histories (e.g., crustal shortening, extension and plate flexure) also exists, which is crucial for extricating signals of sub-plate support from geological observations (e.g., *DeCelles*, 1994).

Available stratigraphic observations include paleo-water depth information recorded in the Paleobiology Database (PBDB), developed by the paleobiological community, and stratigraphic data that record transitions from marine to terrestrial deposition (e.g., *Hintze and Kowallis*, 2009). These data have the important benefit of requiring few corrections, bar minor, relatively well constrained adjustments for compaction and denudation (see, e.g., *Fernandes & Roberts*, 2021). There are of course many other indirect constraints on lithospheric vertical motions including thermochronometry, palynology, isotope altimetry, histories of sedimentary flux, stratigraphic hiatuses, and landform geometries, which can be used to fill in spatio-temporal stratigraphic gaps (e.g., *Blum and Pecha*, 2014; *Chamberlain et al.*, 2012; *Fernandes et al.*, 2019; *Flowers et al.*, 2008,0; *Flowers and Farley*, 2012; *Galloway et al.*, 2011; *Hayek et al.*, 2020,0; *Huntington et al.*, 2010; *Roberts et al.*, 2012; *Vilacís et al.*, 2022). However, we think it is important to make a distinction between information provided from such approaches and the more direct constraints on elevation, uplift and subsidence that arise from interrogating the stratigraphic archive. One of the main advantages of using this approach is that it can provide information about the magnitude and history of net vertical motions, without recourse to proxies or independent information (e.g., lapse rates, geotherms, interpolation, erosional models). It is of course limited to constraining net vertical motion and by the loci of preserved stratigraphy.

In the following sections, first, existing geological constraints on the history of vertical motions of the North American Western Interior are summarized. Secondly, predictions of dynamic topog-

raphy from mantle circulation models are compared to geological observations. We identify model parameterizations that best match geological observations. Similar to a variety of other geodynamic studies, the dynamic topography predictions we make use of were generated without including the shallowest few hundred kilometers of the mantle (e.g., *Flament et al.*, 2013; *Müller et al.*, 2018; *Young et al.*, 2022). Thus, thirdly, geophysical observations of the upper mantle are combined with isostatic models to explore asthenospheric and lithospheric contributions to uplift in the region. The isostatic models we develop make use of seismological and stratigraphic observations to explore contributions to North American topography from asthenospheric thermal anomalies and modification of lithospheric depletion and structure. Finally, we quantify uncertainties and sensitivities via Monte Carlo error propagation, and discuss the implications of our findings for assessing predictions of dynamic topography from geodynamic models.

## 1.2 Global observations of sub-plate support

Potential field and seismological observations combined with magmatism, geomorphology and stratigraphy have been used to quantify modern sub-plate support and histories of dynamic topography (e.g., *Gurnis*, 1990; *Gurnis et al.*, 2000; *Roberts et al.*, 2012; *Klöcking et al.*, 2018; *Stephenson et al.*, 2019; *Ball et al.*, 2021). The relative simplicity and consistency of oceanic lithospheric structure and rheologies, combined with increasingly tightly constrained thermal histories, make it well suited for identifying signals of sub-plate support. For example, the age and isostatically corrected basement depths of oceanic basins have been used to measure residuals from ocean plate cooling models with amplitudes up to  $O(1)$  km (e.g., *Menard*, 1969; *Crough*, 1983; *Panasyuk & Hager*, 2000; *Hoggard et al.*, 2016; *Richards et al.*, 2020; *Valentine & Davies*, 2020). A recent, extensive, compilation of measurements across all oceanic basins indicates that residual surface deflections are measurable to wavelengths at least as low as  $\sim 900$  km (spherical harmonic degree 40; *Holdt et al.*, 2022). These near global-scale compilations of residual topography paint a detailed picture of the present-day state of dynamic topography along continental margins and within oceanic basins. The power spectra of oceanic residual depths indicate that both deep mantle flow and shallower processes, likely involving interaction between the asthenosphere and lithosphere, are fundamental for generating Earth's dynamic surface response. Deep mantle flow primarily contributes to dynamic topography at long wavelengths ( $\sim 10^4$  km), and shallower processes control shorter wavelength contributions ( $10^2$ – $10^3$  km; *Parsons & Daly*, 1983; *Colli et al.*, 2016; *Richards et al.*, 2020). As an example, consider Atlantic oceanic lithosphere abutting eastern North America, which has residuals of up to  $\pm 1$  km (*Holdt et al.*, 2022). Backstripping of stratigraphy preserved along this passive margin indicates that sub-plate drawdown generated 500–900 m of water-loaded subsidence during the last  $\sim 20$  Ma (*Morris et al.*, 2020).

Global compilations of melt fractions of young (Neogene-Quaternary) mafic rocks and upper mantle shear wave velocity anomalies have recently been shown to be broadly negatively correlated (*Ball et al.*, 2021). For example, mafic samples in western North America are concentrated atop slow upper mantle shear-wave velocity anomalies. Many continental regions underlain by relatively slow upper mantle shear wave velocity anomalies, including Western North America, are also associated with uplifted marine rock (*Fernandes et al.*, 2019). Such stratigraphy, preserved atop continental interiors and on fringing sedimentary basins, provides opportunities to constrain histories of sub-plate support (*Fernandes & Roberts*, 2021). Elevated Quaternary marine terraces and warped shorelines provide the least equivocal constraints on vertical lithospheric motions, but are limited to the more recent geological past (e.g., *Austermann et al.*, 2017). Older paleo-water depth indicators preserved in the marine rock record can be used to extend these constraints further into the geological past (e.g., *Dickinson et al.*, 1988; *Bessin et al.*, 2017). A general challenge is generating observations at sufficient scale and density to directly constrain histories of sub-plate support at  $O(10^2$ – $10^3)$  km wavelengths. Building on the methodologies developed by *Ziegler et al.* (1985), *Sahagian* (1988) and *Rowley et al.* (2013), *Fernandes & Roberts* (2021) generated an inventory of 24,372 measurements of Late Cretaceous to Recent net uplift. These measurements were generated by combining records of Cretaceous to Recent marine rock documented in the Paleobiology Database (PBDB) with estimates of elevation, paleobathymetry, compaction, and global sea level change. The distribution of recorded marine rock is of course not uniform across all continents. Nonetheless, most con-

170 tinent have stratigraphic observations preserved in sedimentary basins and atop uplifted topogra-  
171 phy that are suited to testing predictions of geodynamic models.

### 172 1.3 Geodynamic modeling

173 A variety of methodologies exist to retrodict mantle convection. A widely used approach in-  
174 verters mantle structure derived from seismological (tomographic) models of Earth's interior, and can  
175 incorporate supplementary information (e.g., plate motion histories). Methods for prescribing tem-  
176 perature, density and viscosity fields, and also surface velocities, that drive mantle convection sim-  
177 ualations vary (see e.g., *Hager & Richards*, 1985; *Gurnis*, 1990; *Forte*, 2000; *Forte et al.*, 2007; *Forte*  
178 *et al.*, 2009; *Forte et al.*, 2010; *Spasojević & Gurnis*, 2012; *Flament et al.*, 2013; *Müller et al.*, 2018;  
179 *Ghelichkhan et al.*, 2021). As such, associated models have differing predictive capabilities. Some  
180 constrain the present-day state of the mantle and its rate of change, whilst those generated using  
181 backwards advection, adjoint or data assimilation methods make predictions of how dynamic topog-  
182 raphy has changed in the geological past (see, e.g., *Ghelichkhan et al.*, 2021). We note that a sig-  
183 nificant number of mantle convection simulations do not include the shallowest 200–350 km of the  
184 mantle in part because of the computational challenges associated with accurately modeling large  
185 changes in viscosity between the lithosphere and asthenosphere, uncertain lithospheric structure and  
186 rheologies, and difficulty of accurately incorporating boundary layer dynamics on numerical simu-  
187 lations. This approach makes it challenging to ascertain the role the dynamic shallow mantle plays  
188 in generating topography. Given that simulations of mantle convection are often extremely compu-  
189 tationally expensive, we think it is prudent to develop strategies to identify existing simulations that  
190 are consistent with available observations.

191 Here, we focus on testing predictions generated by *Müller et al.* (2018) because they examined  
192 a diverse range of parameterizations, and made their predictions available for testing. We use their  
193 outputs in a plate reference frame. Some of their models incorporate backwards advection, suppress  
194 the formation of plumes, and do not incorporate the shallowest few hundred kilometers into predic-  
195 tions of dynamic topography. As they discuss in their paper, such approaches may reduce the re-  
196 alism of predicted dynamic topography, especially at shorter wavelengths. A focus of this study is  
197 on examining whether contributions from the uppermost convecting mantle and lithosphere, which  
198 might include isostatic effects associated with heating asthenosphere and changes in lithospheric man-  
199 tle thickness or density, are crucial for generating observed vertical lithospheric motions (e.g., *Colli*  
200 *et al.*, 2016). First, we explain why Western North America was chosen to test model predictions.

## 201 2 North American dynamic topography: Observations and theory

### 202 2.1 Geophysical and stratigraphic framework

203 A considerable body of geophysical and geological data across North America constrains the  
204 present-day state of its crust, lithospheric and sub-lithospheric mantle, and therefore isostatic con-  
205 tributions to topography, with higher fidelity than most places on Earth. These include, but are not  
206 limited to USArray-derived seismic velocities of the crust and mantle, active source seismology, grav-  
207 ity anomalies and associated estimates of elastic thickness and dynamic support, and stratigraphic  
208 observations (see, e.g., *Crough*, 1983; *Laske et al.*, 2013; *Buehler & Shearer*, 2016; *Fernandes & Roberts*,  
209 2021; *Hoggard et al.*, 2021). Additionally, isotopic paleoaltimetry, thermochronometry, sedimentary  
210 flux histories, mafic melting histories, and geomorphic observations and theory provide contextual  
211 information about the evolution of North American topography and sub-plate support (see, e.g., *Fer-*  
212 *nandes et al.*, 2019, for summary). Inverse modeling of longitudinal river profiles provides one way  
213 to fill spatio-temporal gaps between spot measurements (e.g., *Roberts et al.*, 2012; *Fernandes et al.*,  
214 2019). Nonetheless, disentangling tectonic (e.g., shortening, extension) and sub-lithospheric contri-  
215 butions to elevations is especially fraught along the western continental margin where tectonic pro-  
216 cesses and terrane accretion have dominated its recent geological history. Instead, we focus on Cre-  
217 taceous to Recent stratigraphy in the North American Western Interior (Figure 1).

218 In our view, the least equivocal, most direct, constraints on histories of North American ver-  
219 tical lithospheric motion arise from the distribution of ancient marine rock (e.g., *Ziegler et al.*, 1985).

Biostratigraphic information contained within these rocks (e.g., age, paleo-water depth) provide crucial clues about the elevation of Earth's surface at specific times, typically when it is at, or close to, contemporaneous sea level. By combining these data with their compaction and denudation histories, spot measurements of post-deposition uplift can be generated for substantial tracts of North American topography (*Fernandes & Roberts*, 2021). The present-day elevation of marine fossil assemblages recorded in the PBDB, for example, provide constraints on post-Cretaceous net uplift in the Great Plains, Rocky-Mountains-Colorado-plateau, Basin and Range, and Interior Lowlands (Figure 1). In addition, stratigraphic sections throughout North America record facies transitions from marine to non-marine depositional environments, which can be used to calculate precise rates of net uplift (e.g., *Hintze and Kowallis*, 2009; *Hampson*, 2010). Building on the body of stratigraphic observations generated by *Crough* (1983), *Ziegler et al.* (1985) and others, *Fernandes et al.* (2019) compiled 339 locations where such stratigraphic transitions are observed in outcropping stratigraphy of the North American Western Interior. Stratigraphy from these locations typically feature as part of well-established chronostratigraphic frameworks that include radiometric dating (*Obradovich & Cobban*, 1975; *Cobban et al.*, 2006; *Merewether et al.*, 2011; *Merewether & McKinney*, 2015; *Lynds & Slattery*, 2017). Thicknesses and distributions of Cretaceous rocks from outcrop and well data (e.g., Mancos Shale) are of special importance because of their role in defining when marine conditions likely last prevailed across large tracts of the continental interior (*Bond*, 1976; *Cross and Piliger*, 1978; *Roberts & Kirschbaum*, 1995; *Li & Aschoff*, 2022).

The subsidence history of the region is also well documented from well and outcrop data. Tectonic processes (lithospheric shortening, extension, plate flexure) evidently generated Cretaceous to Recent accommodation space and uplifted sedimentary rock (e.g., in the Basin and Range province, Rio Grange Rift, Sevier-Laramide piggy-back basins and forelands; *Cross and Piliger*, 1978; *Cross*, 1986; *Dickinson et al.*, 1988; *Dickinson*, 2004). For example, during Cretaceous flooding  $> 12$  km of sediment was deposited in small, isolated, probably flexural basins (e.g., *Roberts & Kirschbaum*, 1995). Nonetheless, the distribution of uplifted marine rock and subsidence patterns indicate that such tectonic processes cannot explain  $O(1)$  km subsidence at horizontal scales  $> 1000$  km. Instead, mantle convective drawdown likely played an important role in generating accommodation space at these scales (e.g., *Mitrovica et al.*, 1989; *Pang & Nummedal*, 1995). In this paper we explore how such observations of net vertical lithospheric motion can be used to assess predictions from geodynamic models.

## 2.2 Quantifying net vertical motions from stratigraphy

### 2.2.1 Uplift

We quantify uplift using the data compilations of marine fossil assemblages with a known paleo-water depth, and stratigraphic markers of the youngest outcropping transition between marine and non-marine depositional environments presented in *Fernandes et al.* (2019) and *Fernandes & Roberts* (2021). Together, these constraints comprise  $> 2000$  spot measurements of net uplift. Regressive stratigraphic sequences were identified from published facies interpretations (e.g., *Roberts & Kirschbaum*, 1995; *Johnson et al.*, 2002; *Gani et al.*, 2015), and ages were tied using published regional chronostratigraphy (Figure 1D; *Obradovich & Cobban*, 1975; *Cobban et al.*, 2006; *Merewether et al.*, 2011; *Merewether & McKinney*, 2015; *Lynds & Slattery*, 2017). Particular care was taken to identify lateral and temporal variability in the depositional facies sequences. Depositional environments, interpreted using fossil assemblages, were converted to paleo-water depth using the paleo-bathymetric model described by *Fernandes & Roberts* (2021, Figure 1E). Elevations and paleo-sea level ranges were extracted from ETOPO1 and the compilation of *Bessin et al.* (2017), respectively.

A demonstration of the methodology for estimating net surface uplift,  $U$ , from fossil assemblages is shown in Figure 2. This figure shows uplift of a fossil assemblage from the Book Cliffs Utah corrected for paleo-water depth, eustatic sea level and compaction. Uplift is calculated simply by incorporating measured modern elevations of fossil assemblages,  $E$ , paleobathymetry,  $B$ , sea level at the time of deposition,  $S$ , a correction for post-depositional compaction,  $\Delta C$ , and their associated uncertainties ( $\delta E$ ,  $\delta B$ ,  $\delta S$ ,  $\delta \Delta C$ ). Such that  $U = E + B - S + \Delta C$  and  $\delta U = [(\delta E)^2 + (\delta B)^2 + (\delta S)^2 + (\delta \Delta C)^2]^{1/2}$ . Global eustasy and paleo-water depths are usually the largest sources of un-

certainty, nonetheless they rarely exceed a few hundred meters for the assemblages used in this study (see *Fernandes & Roberts*, 2021, for extended methodology and the inventory of uplift constraints and calculated uncertainties). Net dynamic topography extracted from Model M2 of *Müller et al.* (2018) is also shown in Figure 2 to illustrate our approach to extracting commensurate (in time) predictions.

The spatial and temporal distribution of paleo-biological data provide constraints on the magnitude of net uplift experienced at each location, and paleo-elevation of the surface at the time of deposition. This information constrains both the absolute paleo-elevation of the region, as well as the magnitude and polarity of net post-deposition vertical motion. Using such inventories of geological observations means that suites of spot measurements can be used to identify vertical motions associated with changes in elevation at the scales predicted by mantle convection models (e.g.,  $> 1000$  km; i.e., larger than deflections determined by flexural rigidity of the lithosphere). The fossil and stratigraphic dataset we make use of covers  $3500 \times 2350$  km, with a sample density of  $\sim 1$  sample per  $\text{km}^2$  in the densest regions (Figure 1D).

There are a variety of means to assess long wavelength contributions to measured uplift (e.g., fitting spherical harmonic functions to spot measurements; *Hoggard et al.*, 2016). Given that we focus on a single continental region, a simple way to do so is to fit splines to spot measurements. We seek gridded surfaces that require the least smoothing of data and allow the amplitude of measurements to be preserved (Figure 1). The resultant grid was filtered using a 1000-km low-pass Gaussian filter and is shown in Figure 3A. A histogram showing the difference between the grid and spot measurements of uplift is shown in Figure 3B. Most spot measurements record a dominantly large-scale,  $> 1000$  km, uplift signal, shown by a difference of less than  $\pm 200$  m for  $> 65\%$  of the spot measurements. Small-scale deviations from the large-scale pattern of uplift are generally associated with tectonic structures generated principally during Laramide deformation and basin-forming tectonic events (see, e.g., *Dickinson et al.*, 1988; *DeCelles*, 2004). Grids generated using alternative low-pass cut-offs are shown in Supplementary Figure S2.

### 2.2.2 Subsidence

Additional constraints on the vertical motions of Western North America were provided by the subsidence history of the Western Interior Basin. Basin stratigraphy recorded in individual wells has been flexurally backstripped to reveal a spatially and temporally variable subsidence pattern (see Supplementary Figures S4–6; *Liu et al.*, 2014). However, individual wells do not constrain the history of subsidence on a sufficiently large scale to accurately reflect the broader geodynamic history of the basin. In order to expand this dataset to larger spatial scales, following *Mitrovica et al.* (1989), we calculate subsidence by backstripping existing regional isopach maps. First, isopach maps from *Roberts & Kirschbaum* (1995) were digitized using QGIS software. The published isopach figures for each time slice were geo-referenced, and contour lines were individually traced to create a vector map of the contour lines where the thickness value of each line is an attribute. Next, using GRASS functionalities, the vector map was rasterized by creating a  $10 \times 10$  minute grid, where each grid cell is either a contour line cell (containing the sediment thickness value), or a fill cell. Using the `r.surf.cont` functionality, a linear interpolation between contour intervals was performed using a flood fill algorithm. Gridding by fitting a regularized spline with tension was also tested, however this methodology produced unwanted data artifacts in regions where the contour lines were too closely spaced. The best-fit isopach maps are shown in Supplementary Figure S4.

Air-loaded subsidence histories were calculated by backstripping the isopach maps. Admittance between gravity and topography, and their associated coherence, indicates that the elastic thickness of the lithosphere,  $T_e$ , beneath the North American Western Interior is  $< 40$  km and as low as  $\sim 10$  km atop the Colorado Plateau (*Stephenson et al.*, 2014; *Audet*, 2014). These results suggest that it is reasonable to assume isostasy prevails when backstripping. The isopach maps were decompacted using the compaction parameterisation of *Athy* (1930). We assumed a compaction wavelength  $\lambda = 2$  km and initial porosity  $\phi_0 = 0.6$ , typical for sandstones (*Sclater & Christie*, 1980). Minimum and maximum subsidence was calculated by assuming 0 and 3 km thickness of post-Cretaceous sediment was preserved atop Cretaceous rock, respectively. Maximum thickness of post-Cretaceous rocks were

estimated from average thicknesses preserved in boreholes and outcrops in the area (e.g., *Hintze and Kowallis*, 2009). In order to compare the subsidence histories with dynamic topography predictions, decompacted subsidence was isostatically air-loaded assuming a density of sedimentary rock,  $\rho_s = 2400 \text{ kg m}^{-3}$ . The resultant grids of calculated subsidence are shown in Supplementary Figure S5 and are summarized for specific localities of interest in Figure 6. These maps are in broad agreement with previous studies, providing a large-scale spatio-temporal history of subsidence (see *Cross and Piliger*, 1978; *Mitrovica et al.*, 1989). The pattern and magnitude of subsidence predicted from this simple method was compared to subsidence estimates for the same time intervals generated from backstripping of data from individual wells (colored circles in Figure 6; *Liu et al.*, 2014). There is generally a good agreement between the well data and the subsidence grids, both in the spatial distribution and the magnitude of subsidence.

The results suggest that parts of the westernmost portion of the study region, i.e., the Basin and Range and Colorado Plateau, experienced subsidence due to lithospheric thinning and loading. Backstripping of well data predict a higher magnitude of subsidence in the Late Campanian, which is likely due to a combination of grid smoothing and choice of compaction parameterisation. We now have a body of uplift and subsidence data from across Western North America with which we can test predictions from geodynamic simulations of mantle convection.

### 3 Testing histories of dynamic topography from mantle convection simulations

#### 3.1 Introduction

A substantial body of published mantle convection simulations predict dynamic topography of Western North America (see, e.g., *Forte et al.*, 2007; *Liu et al.*, 2008; *Mouha et al.*, 2008; *Forte et al.*, 2009; *Flament et al.*, 2013; *Liu et al.*, 2014; *Rovere et al.*, 2015; *Müller et al.*, 2018; *Davies et al.*, 2023). We focus on testing predictions of dynamic topography from the seven models presented by *Müller et al.* (2018). Their paper describes their methodologies in depth and clearly explains challenges and potential pitfalls in comparing model predictions to independent geologic observations. An important issue they discuss, which we address below, is exclusion of the upper few hundred kilometers of the Earth from calculations of dynamic topography. In short, they test different parameterizations including variations in viscosity, thermal expansivity, density, activation energies and initial conditions. They also test models that contain plumes and models in which plume formation is suppressed. The models can be placed into three categories based on their parameterizations, each of which make broadly similar predictions: M1, M2–M4 and M5–M7. In model M1 mantle flow is computed by a backwards integration of the temperature field wherein the direction of gravity and plate motions are reversed (*Liu et al.*, 2008; *Spasojević & Gurnis*, 2012). The other models are driven by forward thermal convection with plate velocities applied as surface boundary conditions using a modified version of CitcomS (*Müller et al.*, 2018). The main difference between the M2–M4 and M5–M7 families of models lies within their viscosity structures; M5–M7 models have mantle viscosities that are lower by  $O(10\text{--}10^2)$ , and a much larger viscosity contrast between the lithosphere and asthenosphere (asthenosphere viscosity being  $500\times$  lower, when compared to  $10\times$  lower in models M2–M4). For all models, average model resolution is  $50\times 50\times 15 \text{ km}$  at Earth's surface. Predicted dynamic topography and its incremental change for each model is shown in the Supplementary Information.

Examples of predicted net change in dynamic topography from each category are shown in Figure 4A–C. Grids of calculated net dynamic topography were generated by subtracting values from a specific time in the past (e.g., 90, 80, 70 or 60 Ma) from present-day values (see, e.g., Figure 4A). By doing so we can compare changes in predicted dynamic topography to net uplift or subsidence recorded by stratigraphy. Each group of models generated significantly different predictions of the history, spatial distribution and amplitude of dynamic topography. We compare absolute elevations and net vertical motions recorded by stratigraphy to predictions of net dynamic topography.

372      **3.2 General insights from testing geodynamic predictions using geologic observa-**  
 373      **tions**

374      Müller *et al.* (2018) compared their dynamic topographic predictions to power spectra of ocean-  
 375      age depth residuals and to paleo-geographic maps generated by, e.g., Smith *et al.* (1994) and Heine  
 376      *et al.* (2015). Most of the models over-predict power calculated from ocean-age depth residuals at  
 377      spherical harmonic degrees 1–2 (wavelengths  $\approx 2.2 \pm 0.6 \times 10^4$  km; see their Figure 5), despite hav-  
 378      ing excised the top 300 km of the upper mantle, which contain strong long-wavelength anomalies.  
 379      Models M5–7 most closely match spectra of residual depth anomalies at degrees 2–3 ( $\lambda \approx 1.4 \pm$   
 380       $0.3 \times 10^4$  km), but under-predict power at higher degrees. Models M1–4 more closely match at de-  
 381      grees 3–5 ( $\lambda \approx 0.9 \pm 0.2 \times 10^4$  km). In other words, none of the models match the entire power  
 382      spectrum of ocean age-depth residual at degrees 1–5, but some provide a reasonably good fit at spe-  
 383      cific scales. Paleo-geographic maps were also used to identify regions submerging or emerging with  
 384      respect to sea level at given time periods. These data were used to constrain the polarity of verti-  
 385      cal lithospheric motions (i.e., uplift or subsidence). Their preferred model, which most closely matches  
 386      continental inundation by seaways, is the forward geodynamic simulation M7, which suppresses plumes.  
 387      We explore whether amplitudes and net change in vertical lithospheric motion provide additional  
 388      useful information to discriminate between models. In this study, we test the model predictions us-  
 389      ing geological observations in three ways.

390      First, amplitude and polarity of net dynamic topographic change since the Late Cretaceous  
 391      are compared to spot measurements from the PBDB augmented by 339 spot measurements that tightly  
 392      constrain the timing of transition from marine to terrestrial conditions. We select eight specific lo-  
 393      calities with different tectonic and lithospheric settings across the continent to demonstrate our ap-  
 394      proach (Figures 1, 10, S3). The seven geodynamic models predict net uplift for most of the North  
 395      American Western Interior since the late Cretaceous, however the pattern and amplitude of uplift  
 396      significantly vary between models. As an example of the diversity of model predictions, consider Fig-  
 397      ure 4D–G, which shows calculated dynamic topography in Alberta, Manitoba, Utah and New Mex-  
 398      ico (see Figure 4A). Predicted net dynamic topography was extracted at the same location and for  
 399      the same duration as each PBDB and stratigraphic constraint (see, e.g., Figure 2).

400      Second, predictions of the absolute amplitude of dynamic topography in the Late Cretaceous  
 401      are compared to paleo-water depth estimates from the PBDB and additional stratigraphic constraints.  
 402      Air-loaded predictions of dynamic topography from the geodynamic models ( $D_{air}$ ) were isostatically  
 403      corrected to a water-load ( $D_w$ )

$$D_{air} = D_w \frac{\rho_a}{\rho_a - \rho_w} \approx 1.43 D_w. \quad (1)$$

404      where  $\rho_a$  and  $\rho_w$  is the density of asthenospheric mantle and water, respectively. To extract predicted  
 405      water-loaded dynamic topography at a specific time (e.g., the time of deposition of the fossil assem-  
 406      blage in Figure 2, 81.22 Ma) the discrete time steps (e.g., 80, 90 Ma) of Müller *et al.* (2018) were  
 407      linearly interpolated (see blue line in Figure 2D). Thus, predicted dynamic topography at the lo-  
 408      cation and time of deposition of each fossil assemblage was extracted and compared to the observed  
 409      paleo-bathymetry (interpreted from the fossil record).

410      Finally, the history of Late Cretaceous dynamic topographic vertical motions are compared  
 411      to the subsidence history of the Western Interior Basin. Figure 6 shows the Late Cretaceous ver-  
 412      tical motions at four key locations (shown in Figure 4A). For each location, the first panel shows  
 413      paleo-water depth of fossil assemblages located within a 50 km radius of dynamic topography pre-  
 414      dicted by the geodynamic models. The second panel shows the predicted net change in dynamic to-  
 415      polography for each Late Cretaceous stage: Cenomanian, Turonian, Santonian–Coniacian, lower Cam-  
 416      panian, upper Campanian and Maastrichtian. The final panel shows the range of isopach thicknesses  
 417      within a 50 km radius of the point, isostatic subsidence from backstripping the isopach maps of Roberts  
 418      & Kirschbaum (1995), and a subsidence curve from Liu *et al.* (2014). In all cases, the continuous  
 419      subsidence of the Western Interior Basin in the Late Cretaceous requires that the net vertical mo-  
 420      tion of the surface is negative. However, with the exception of point 8, located in the eastern-most

edge of the Western Interior Basin, all models predict dynamic uplift of the North American Western Interior in the Late Cretaceous.

In the following subsections we summarize the specific parameterizations, described in detail by Müller *et al.* (2018), and predictions from each group of models. The fidelity of predicted dynamic topography is then assessed by comparison to the inventory of stratigraphic data.

### 3.3 Geodynamic Model M1

Model M1 uses the plate reconstruction of Gurnis *et al.* (2012), and is equivalent to the hybrid model of Spasojević & Gurnis (2012, their model M2). The global mantle temperature field at present-day is estimated using tomographic inversions of different seismic phases (surface and body waves using the S20RTS model in the lower mantle, and Benioff zone seismicity for the upper mantle). The temperature field is back-integrated using the backward integration method of Liu & Gurnis (2008). A hybrid paleo-buoyancy field is generated by merging the calculated backward-advection mantle temperature field with synthetic subducted slabs assimilated into the model based on location of subduction zones (Spasojević & Gurnis, 2012). The model has a Rayleigh number,  $Ra = 7.5 \times 10^7$ . Air-loaded dynamic topography is calculated with a no-slip surface boundary condition, with the top 250 km of mantle removed from the calculation. The power spectra of dynamic topography predictions show that model M1 has the highest power at spherical harmonic degree  $l = 1 - 3$  for all examples considered by Müller *et al.* (2018). It predicts highest amplitudes of dynamic topography at wavelengths  $> 10,000$  km. Comparisons between observed and predicted net vertical motions since  $85 \pm 5$ ,  $75 \pm 5$ ,  $65 \pm 5$  and  $< 60$  Ma are shown in Figure 5A. For each scatter plot, a linear regression was fit using a least-squares residual misfit calculation. Model M1 tends to under-predict net uplift of Cretaceous to earliest Cenozoic marine rocks. Observed and predicted paleo-water depths for model M1 are shown in Figure 5E–H, along with a least-squares regression fit through the data. The range of predicted Cretaceous to Cenozoic water-loaded elevations is somewhat larger than those constrained by biostratigraphic data. However, we note that many of the points coincide with the 1:1 line within error.

### 3.4 Models M2–M4

Models M2–M4 are characterized by initial conditions that include a 113 km thick basal thermochemical layer above the core-mantle boundary (CMB) that is 4.2% denser than ambient mantle, which acts to suppresses plume formation. This dense basal layer has the same thickness as the lower thermal boundary layer. They explore the consequences of assuming constant thermal expansion and temperature-dependent viscosity. The models have a  $Ra = 7.8 \times 10^7$ . Model M2 uses the plate reconstruction of Seton *et al.* (2012), and is equivalent to Model 3 from Müller *et al.* (2016a). Model M3 uses the plate reconstruction of Müller *et al.* (2016a) and is equivalent to Model 2 described in Müller *et al.* (2016a). Model M4 uses the relative plate motions of Müller *et al.* (2016a), absolute plate velocities of Van der Meer *et al.* (2010), and is equivalent to model (case) 24 from Flament *et al.* (2017).

For models M2–4 (and M5–7), dynamic topography is calculated from surface vertical stress resulting from mantle flow in restarts of the model in which the surface boundary condition is free-slip and top 350 km is removed from the calculations. Lateral viscosity variations are preserved in the rest of the mantle. The power spectra of predicted dynamic topography from all models show that for models M1–M4 the highest power resides at spherical harmonic degree  $l = 2$ .

The amplitude of observed net uplift is best matched by models M2, M3 and M4 (see Figure 5C). These models predict a large amplitude drawdown at  $\sim 90$  Ma, ranging from  $-1.5$  km to  $-4$  km, and subsequent net uplift to  $\sim 0$  km at present day. Uplift is highest in the West (Arizona, Colorado, Wyoming) with a smooth decrease to the East (Illinois, Wisconsin). If all of the uplift was dynamic in origin, these results would suggest that the present-day topography of the North American Western Interior may not be dynamically supported, but instead owes its history of vertical motions to recovery from Cretaceous drawdown caused by subduction of the Farallon slab (Spasojević & Gurnis, 2012). As such, any additional sources of vertical motions would be negligible. Models

M2–M4 predict as much as 1.5 km of uplift near the Colorado Plateau (near the Utah–Colorado border) during Santonian–Coniacian times (83.6–89.8 Ma). Conversely, the stratigraphic record indicates water-loaded subsidence of  $\sim 100$ –500 m and up to 1.5 km of sediment accumulation during this time. As far as we are aware, there is no evidence for a widespread stratigraphic unconformity that might be expected to have been generated as a consequence of 1.5 km of regional uplift during this time.

M2–M4 predict up to  $\sim 1$  km of water-loaded Cretaceous subsidence, with a sharp uplift pulse (with magnitude up to 1.5 km) between 90–70 Ma that is not observed in the paleo-water depth record. In general the amplitude of elevations predicted from the geodynamic models (up to  $-4$  km) overestimate observed, mostly neritic,  $O(10)$  m, paleo-water depths.

### 3.5 Models M5–7

Models M5–M7 are based on examples presented in *Hassan et al. (2015)* and *Barnett-Moore et al. (2017)*. Plumes are present in models M5–6 due to a 100 km thick, 2.5% denser basal thermochemical layer above the core–mantle boundary that is thinner than the basal thermal boundary layer (300 km). Like models M2–M4, M7 contains a 113 km basal thermochemical layer above the core–mantle boundary made of 10% denser than ambient mantle, which suppresses plume formation. All models assume a mantle adiabat, where thermal expansion is set to decrease with depth (i.e., background mantle temperature is depth-dependent). They have an initial potential temperature of 1252°C and a temperature drop of 952°C between thermal boundary layers. Viscosity variation with temperature is parameterized using Arrhenius laws. The models incorporate viscous dissipation and adiabatic heating, internal radiogenic heating, and have a  $Ra = 5 \times 10^8$ . Model M5 is equivalent to model M3 developed by *Hassan et al. (2015)* and incorporates the plate reconstruction of *Seton et al. (2012)*, with modifications for the Arctic from *Shephard et al. (2013)*, and modified absolute plate motions from *Shephard et al. (2014)*. Model M6 uses plate reconstructions of *Müller et al. (2016a)* and *Müller et al. (2016b)* and is equivalent to model C1 of *Barnett-Moore et al. (2017)*.

Models M5–M7 have highest power at degree  $l = 1$ . Power drops off by more than an order of magnitude between  $l = 3$  and 5. Models M5–M7 significantly under-predict the amplitude of net uplift. Nor can these models fully explain the large-scale surface tilt of the North American Western Interior. Conversely, the absolute amplitudes of models M5–M7 tend to match observed paleo-water depth within error. An important consideration is that sediment infill of accommodation space generated by dynamic drawdown could result in the maintenance of shallow paleo-water depths. This hypothesis can be investigated using the history of basement subsidence and sediment accumulation in the Western Interior Basin (e.g., Figure 6).

### 3.6 Summary of predicted dynamic support, observations and next steps

The predictions of dynamic topography from models M1–M7 are successful at recreating the broad patterns of uplift and drawdown of the North American Western Interior. Similarly, they have been shown to agree with broad patterns of continental inundation estimated using the fossil record (*Müller et al., 2018*). However, some substantial discrepancies between the geological record of large-scale vertical motions and predictions from geodynamic models exist. For instance, predicted dynamic topography is inconsistent with amplitudes and polarities of net post-Cretaceous vertical motions in the North American Western Interior (Figures 4–6). Similarly, predicted paleo-bathymetries of the Western Interior Basin also tend to be discrepant (Figure 4). It is intriguing that models that predict paleo-bathymetry with some fidelity tend to be poor predictors of net changes in vertical motions, and vice versa (e.g., Figure 5). As *Müller et al. (2018)* discuss, an obvious source of discrepancy between observations and model predictions is excising contributions from the lithosphere and uppermost convecting mantle (uppermost 250–350 km) from predictions of vertical motions, which is common practice in such studies (see, e.g., Section 3.1).

Increasingly comprehensive seismological, magmatic and potential field observations are beginning to generate coherent views on the thickness and density of North American lithosphere, which simplifies isolation of sub-plate support (e.g., *Ball et al., 2021; Buehler & Shearer, 2016; Hoggard*

et al., 2021). Thus, in the rest of this paper, we seek to establish whether relatively simple isostatic calculations and geophysical observations of the uppermost convecting mantle and lithosphere beneath North America can be used to reconcile discrepancies between predictions from Models M1–M7 (that incorporate deeper structure) and the observations. We then finish this paper by briefly discussing alternative approaches to predict dynamic support and how they might be tested using the observations.

## 4 Assessing Shallow Mantle Contributions to Modern Topography

It is well known that uplift and subsidence at, or close to, Earth's surface are often dominated by the thermal and structural evolution of the lithosphere (e.g., Watts, 2001). Changes in asthenospheric buoyancy via thermal expansion also appear to be important contributors to observed patterns of uplift (Parsons & Daly, 1983; Rudge et al., 2008; Hartley et al., 2011; Ghelichkhan et al., 2021). Surface response kernels indicate that the shallow mantle (< 400 km) exerts a key role in controlling evolution of Earth's topography (Parsons & Daly, 1983; Colli et al., 2016; Richards et al., 2020). Calculated sensitivity kernels indicate that the convecting mantle directly beneath the lithosphere–asthenosphere boundary produces the strongest contributions (from the convecting mantle) to topography (e.g., Parsons & Daly, 1983; Colli et al., 2016; Ghelichkhan et al., 2021). These results are supported by instantaneous flow models, which show, first, that topographic deflections caused by internal buoyancy anomalies have amplitudes that are inversely proportional to the depth of the anomaly (Hager & Richards, 1989). Secondly, they indicate that amplitudes of topography closely approximate those expected for full isostatic compensation when they are generated by buoyancy variations in the uppermost mantle (asthenosphere and lithosphere). One of the key outstanding challenges is being able to “see through” isostatic contributions from the crust and lithospheric mantle to test predictions from geodynamic models of mantle convection. Here, we first summarize geophysical and geochemical observations that indicate shallow mantle contributions to the modern elevation of the North American Western Interior. Simple isostatic calculations are then used in conjunction with those insights to estimate contributions to net vertical motions of Cretaceous and younger marine rock from excess asthenospheric temperatures and changes to lithospheric structure.

### 4.1 Geophysical features of shallow North American mantle

Seismic shear-wave velocities ( $V_S$ ) are sensitive to temperature in the upper mantle and provide a useful guide to the thermal state of the lithosphere and asthenosphere beneath continents (e.g., Schutt & Lesher, 2006). Figure 7A shows a slice at 125 km depth through the SL2013sv shear wave velocity model and the location of Late Cretaceous to Recent mafic magmatism (Fitton et al., 1991; Walker et al., 2006; Roy et al., 2009; Schaeffer & Lebedev, 2014; Klöcking et al., 2018). Shear wave velocities show a distinctive spatial pattern, being slow in the west and fast in the east, separated by an undulating boundary. Slow velocities broadly coincide with the location of Late Cretaceous to Recent magmatism, giving complimentary indications of anomalously warm asthenosphere and thin lithospheric mantle (Ball et al., 2021).

To quantify the role of upper mantle temperatures in generating vertical lithospheric motions, the SLNAAFSA  $V_S$  tomography model of Hoggard et al. (2020)—a hybrid which embeds high-resolution regional models for North America (SL2013NA; Schaeffer & Lebedev, 2014), Africa (AF2019; Celli et al., 2020) and the South Atlantic (SA2019; Celli et al., 2020) within the global SL2013sv model of Schaeffer & Lebedev (2013)—is converted to temperature using the methodology of Richards et al. (2020). This approach incorporates recent experimental parameterizations of anelasticity at seismic frequencies (Yamauchi & Takei, 2016), allowing the highly non-linear relationship between  $V_S$  and temperature at near-solidus conditions (e.g., within the asthenosphere) to be accurately constrained. Our best-fitting anelastic parameters for this model differ slightly from those quoted in Hoggard et al. (2020), due to our use of an updated oceanic lithospheric cooling model (Richards et al., 2020, instead of Richards et al., 2018). The parameters controlling the unrelaxed shear modulus,  $\mu_U$ , are  $\mu_0=75.91$  GPa,  $\partial\mu/\partial T = -0.01794$ , and  $\partial\mu/\partial P = 2.538$  (see Richards et al., 2020, their Equation 8), while those controlling the steady-state diffusion creep viscosity and proximity to the solidus

572 are  $\eta_0 = 9.538 \times 10^{22}$  Pa s,  $E_a = 4.889 \times 10^5$  J mol $^{-1}$ ,  $V_a = 6.26 \times 10^{-7}$  m $^3$  mol $^{-1}$ , and  $\partial T_s / \partial z =$   
 573  $0.9309^\circ\text{C km}^{-1}$  (see *Richards et al.*, 2020, their Equations 9 & 11). Note that this parameterization  
 574 is only valid in the upper 400 km of the mantle, since calibrated material properties are appropri-  
 575 ate for an olivine-dominated composition and do not account for phase transitions. In addition, the  
 576 uppermost 50 km is excluded from our analysis to avoid errors associated with downward bleeding  
 577 of crustal velocities to lithospheric depths, a problem that is particularly pronounced in continen-  
 578 tal interiors and leads to unrealistically elevated temperature predictions at shallow depths.

579 Calculated temperatures for the 125 km depth slice are shown in Figure 7B, and other depth  
 580 slices are shown in the Supporting Information (Figure S7). As expected, temperatures follow the  
 581 patterns of the  $V_S$  tomography model, with hottest potential temperatures in the west beneath the  
 582 Basin and Range and Colorado Plateau reaching upwards of  $\sim 1445^\circ\text{C}$ . Mantle temperature estimates  
 583 can be used to map the depth to the lithosphere-asthenosphere boundary (LAB), defined here by  
 584 the  $1200^\circ\text{C}$  isotherm (white dashed line in Figure 7B; Figure S8), which delineates a region of thin-  
 585 ner lithosphere in the west. Note that defining the LAB by the  $1300^\circ\text{C}$  isotherm, as has been done  
 586 in other studies (*Afonso et al.*, 2016), does not significantly change the observed thickness or loca-  
 587 tion of significant gradients in thickness (white solid line in Figures 7B).

588 Figure 7C shows lithospheric thickness as defined by the  $1200^\circ\text{C}$  isotherm, filtered to include  
 589 only spherical harmonic degrees smaller than  $l = 60$  (wavelengths  $> 660$  km; the unfiltered LAB  
 590 is included in the Supporting Information, Figure S7). This filtering approach seeks to remove small-  
 591 scale features that might be a consequence of artifacts in the underlying SLNAAFS tomographic  
 592 model. Comparison of mantle temperature and LAB depths to the observed net uplift shows that  
 593 most of the uplift since the Late Cretaceous has occurred atop lithosphere that is thin compared to  
 594 the interior of the continent and atop asthenosphere that is relatively warm (cf. Figures 1, 3 & 7D).  
 595 The most prominent anomaly is centered on the protuberance of thicker lithosphere beneath the Colorado-  
 596 Utah-Wyoming state borders, where uplift is high yet the lithosphere is thick. This region also co-  
 597 incides with a spatial gap in magmatism, and may indicate a more melt-depleted and viscous litho-  
 598 sphere.

599 Figure 8 shows cross-sections of topography, mantle temperatures and lithospheric thicknesses  
 600 from west to east (see Figure 7B for locations). Topographic data was extracted from the SRTM90  
 601 dataset (*Jarvis et al.*, 2008). Mantle temperatures and lithospheric thicknesses were calculated in  
 602 this study (Figure 7). Crustal thicknesses were extracted from the PnUS model (*Buehler & Shearer*,  
 603 2016). Colored circles and squares show the present-day elevation of PBDB and stratigraphic up-  
 604 lift constraints, respectively. They are shown atop 100 km-wide swath profiles of elevation (see *Fer-*  
 605 *nandes & Roberts*, 2021). Crustal thicknesses (black dashed lines) do not exceed 50 km and show  
 606 no significant variation below topographic gradients. Assuming crustal composition does not vary  
 607 significantly laterally, changes in crustal thickness alone cannot be used to explain the topographic  
 608 gradient (*Roberts et al.*, 2012; *Klöcking et al.*, 2018; *Levandowski et al.*, 2018). On the other hand,  
 609 lithospheric and asthenospheric temperatures show significant lateral variation, and consequently  
 610 so does lithospheric thickness. All cross sections show an increase in lithospheric thickness to the  
 611 east, accompanied by a drop in surface elevations. The magnitude of lithospheric thickness and to-  
 612 graphic change, however, varies significantly from north to south. Cross section X-X', crossing  
 613 the Northern Rocky Mountains, shows LAB depth increasing from  $\sim 125$  km to  $\sim 225$  km from east  
 614 to west, concomitant with a change in the mean elevation of  $\sim 1.6$  km. Moving south to cross sec-  
 615 tion Z-Z', LAB depth increases from  $\sim 80$  km beneath the Southern Rocky Mountains to  $\sim 200$  km  
 616 beneath the eastern Great Plains, accompanied by an elevation difference of  $\sim 2.8$  km. Elevations  
 617 between the Colorado Plateau and the Southern Rockies also have similar changes in shallow man-  
 618 tle temperatures and elevations.

619 The correspondence between upper mantle temperatures and changes in surface elevation sug-  
 620 gests that the uppermost mantle may have played an important role in controlling the evolution of  
 621 topography in the North American Western Interior. We thus combine these geophysical observa-  
 622 tions with simple isostatic models to quantify the contributions of mantle temperature and chang-  
 623 ing lithospheric thickness to the uplift history of the North American Western Interior.

## 624 4.2 Topographic support from asthenospheric thermal anomalies

625 We first assess contributions to topographic support from an asthenospheric channel,  $h$ , that  
 626 sits directly beneath the lithosphere (see Supporting Figure S9). Absolute asthenospheric temper-  
 627 atures,  $T$ , are calculated using the SLNAAFS tomographic model and the  $V_S$  to  $T$  conversion scheme  
 628 summarized in Section 4.1 (Figures 7–8). Prior to calculating support, absolute temperatures are  
 629 converted into potential temperatures. We do so because absolute temperatures vary as function of  
 630 depth,  $z$  (strictly pressure), and we are interested in isolating contributions from thermal anom-  
 631 alies. Potential temperature,  $T_p$  ( $^{\circ}$ C), is related to temperature,  $T$  ( $^{\circ}$ C), such that

$$632 T_p = (T + 273) \exp\left(-\frac{\alpha g z}{C_p}\right) - 273, \quad (2)$$

632 where thermal expansivity  $\alpha = 3.3 \times 10^{-5} \text{ K}^{-1}$ , gravitational acceleration  $g = 9.81 \text{ m s}^{-2}$ , heat  
 633 capacity  $C_p = 1187 \text{ J K}^{-1} \text{ kg}^{-1}$ . Calculated temperatures are used to estimate excess potential  
 634 asthenospheric temperatures,  $\Delta T_p$ . They are calculated by taking the difference between the mean  
 635  $T_p$  for the layer and the background, here  $T_p^{\circ} = 1333^{\circ}\text{C}$ . Support (strictly, uplift relative to refer-  
 636 ence mantle),  $U$ —assuming isostasy prevails—can then be calculated as

$$637 U = \frac{h \alpha \Delta T_p}{1 - \alpha T_p^{\circ}}. \quad (3)$$

637 Note that calculated support is relatively insensitive to the choice of assumed background temper-  
 638 ature (see, e.g., Rudge *et al.*, 2008). Inspection of Equation 3 shows that support is sensitive to chang-  
 639 ing the thickness of the anomalously hot layer and excess temperature; doubling either doubles the  
 640 support. We acknowledge that the thickness of the asthenospheric channel,  $h$ , can be defined in dif-  
 641 ferent ways (e.g., constant depth to the base of an asthenospheric channel, or constant thickness be-  
 642 neath the base of the lithosphere). Mean excess temperatures for different definitions are given in  
 643 the Supplementary Information (Figure S9). Estimated support for layers thicker than  $\sim 100 \text{ km}$   
 644 are likely unreliable because the isostatic approximation underpinning Equation 3 becomes increas-  
 645 ingly less valid with depth and predicted topography begins to significantly overestimate the true  
 646 amplitude of asthenospheric contribution to dynamic topography. Table 1 summarizes the sensitiv-  
 647 ity of calculated support to each parameter in Equation 3 for unit adjustments. Sensitivity of all  
 648 model parameters is explored in Figure 9, which we return to later after lithospheric isostatic cal-  
 649 culations are introduced.

**Table 1.** Support (strictly uplift relative to reference mantle) from heating an asthenospheric layer be-  
 649 neath the lithosphere with thickness  $z_L = 200 \text{ km}$  and background (reference mantle) potential temperature  
 $T_p^{\circ} = 1333^{\circ}\text{C}$  by  $1^{\circ}\text{C}$ .

| Parameter                     | Reference value | $\delta$ | $\Delta U$ (km)       | %                    |
|-------------------------------|-----------------|----------|-----------------------|----------------------|
| $h$ (km)                      | 100             | $\pm 1$  | $3.66 \times 10^{-5}$ | 1.01                 |
| $T_p^{\circ}$ ( $^{\circ}$ C) | 1333            | $\pm 1$  | $1.30 \times 10^{-7}$ | $3.6 \times 10^{-3}$ |
| $z_L$ (km)                    | 200             | $\pm 1$  | $1.04 \times 10^{-6}$ | 0.029                |

650 We can now use stratigraphic data (Figure 3) and mantle temperatures derived from  $V_S$  to-  
 651 mography (Figure 7) to investigate whether the observed elevation of marine rock could be a con-  
 652 sequence of support by asthenospheric heating. First, marine rock elevations were (spatially) aver-  
 653 aged in  $1 \times 1^{\circ}$  bins, which approximates the resolution of the shear wave tomography model. For  
 654 each binned set of elevations, excess potential temperature within a  $100 \text{ km}$  thick layer beneath the  
 655 base of the lithosphere was extracted from the  $T_p$  grid (Figure 7D; Supplementary Information). Binned  
 656 elevations as a function of asthenospheric potential temperature are shown in Figure 10A, with the  
 657 physiographic province of each measurement indicated by color (see Figure 1B for locations and col-  
 658 ors). The distribution of elevations is broadly uniform between 0.5 and 2 km. The distribution of

potential temperatures is unimodal, with cool mantle temperatures in the shallowest 100 km beneath the lithosphere (mostly  $1200 < T_p < 1300^\circ\text{C}$ ), with respect to assumed background mantle temperature  $T_p = 1333^\circ\text{C}$ . Few locations beneath the Colorado Plateau and Basin and Range have calculated shallow mantle potential temperature anomalies exceeding  $1333^\circ\text{C}$ , in agreement with estimates of potential temperatures for the region from basalt geochemistry (*Klöcking et al.*, 2018).

Equation 3 can be used to explore whether observed elevations can be explained by asthenospheric heating alone. The solid black line in Figure 10A shows support (strictly uplift, Equation 3) predicted from heating a 100 km thick asthenospheric layer located immediately beneath the lithosphere–asthenosphere boundary. The isostatic calculation predicts no more than 500 m of uplift from a layer with  $T_p = 1450^\circ\text{C}$  if heating from a background mantle potential temperature of  $1333^\circ\text{C}$  is assumed. If the background mantle temperature is assumed to be significantly cooler, e.g.,  $1200^\circ\text{C}$ , maximum predicted uplift is still less than 1 km. These results indicate that isostatic support from heating of even an anomalously cool asthenospheric mantle alone cannot explain the 2–3 km of observed elevations. At most, ~1 km of uplift of the Colorado Plateau and Basin and Range can be explained by warming of initially cool asthenospheric mantle. Other obvious contributors to isostatic support are lithospheric thicknesses and densities. Thus, in the following subsection we assess the consequences of thermally equilibrated and disequilibrated lithosphere for generating observed patterns of uplift.

#### 4.3 Relations between the lithosphere and elevation of marine stratigraphy

We examine contributions from thermally equilibrated and disequilibrated lithosphere with a view to assessing the range of topographic support that lithospheric mantle could provide to topography. We discuss their geologic implications, with regards to histories of lithospheric thinning, in Section 5. Assuming isostasy prevails, support as a function of thermally equilibrated lithospheric thinning,  $U(\Delta t_L)$ , is given by

$$U(\Delta t_L) = \frac{1}{\rho_a} [t_{L_i}(\rho_{L_i} - \rho_a) + t_{TBL_i}(\rho_{TBL_i} - \rho_a) + (t_{L_i} - \Delta t_L)(\rho_a - \rho_{L_f}) + t_{TBL_f}(\rho_a - \rho_{TBL_f})] \quad (4)$$

where  $t_{L_i}$  and  $t_{L_f}$  is the initial lithospheric thickness,  $t_{TBL_i}$  and  $t_{TBL_f}$  are the initial and final thickness of the thermal boundary layer, respectively. Density of asthenospheric mantle is given by  $\rho_a$ , and the initial and final densities of lithospheric mantle and thermal boundary layer are given by  $\rho_{L_i}$ ,  $\rho_{L_f}$ ,  $\rho_{TBL_i}$ ,  $\rho_{TBL_f}$ , respectively. The depth to the base of the thermal boundary layer,  $z_{TBL}$ , is defined as a linear function of the thickness of the lithosphere, and is given by

$$z_{TBL} = (1.678z_{L_1}) - 5.472, \quad (5)$$

where  $z_{L_1}$  is the depth to the base of the lithosphere. This relationship is derived by analyzing the correspondence between the depth to the  $1200^\circ\text{C}$  isotherm inferred from  $V_S$ -derived geothermal profiles and the depth to the base of the thermal boundary layer obtained by fitting steady-state geotherms to these  $V_S$ -based temperature predictions (see Text S3 and Equation S1 in *Hazzard et al.*, 2023).

In an idealized case, density of the lithospheric mantle, thermal boundary layer and asthenospheric mantle are taken to be a function of temperature. Mantle density,  $\rho_m$ , is calculated as

$$\rho_m = \rho_\circ (1 - \alpha \overline{T_m}), \quad (6)$$

where  $\rho_\circ$  is the reference mantle density at standard temperature and pressure ( $3.33 \text{ Mg m}^{-3}$ ),  $\alpha$  is the mantle thermal expansivity, and  $\overline{T_m}$  is the average temperature of the mantle layer. For lithospheric mantle densities,  $\rho_L$ , compositional variation can be included as  $(1-d)\rho_\circ(1-\alpha\overline{T_a})$  where  $d$  is a lithospheric density depletion factor between 0 and 1. The temperature of the lithospheric mantle is calculated assuming a linear geothermal gradient from the surface, here set to  $0^\circ\text{C}$ , to the base of the lithosphere, defined at the  $1200^\circ\text{C}$  isothermal surface. The temperature of the thermal bound-

699       ary layer is calculated assuming an upper bounding temperature of 1200°C and a basal temperature  
 700       calculated assuming an adiabatic gradient defined by Equation 2. Similarly, temperature of the  
 701       asthenospheric mantle is calculated using the same adiabatic gradient.

702       These equations can be used to propagate uncertainties and to assess the sensitivity of calculated support  
 703       to the properties of the lithosphere. Table 2 shows sensitivity of calculated support  
 704       to unit adjustment,  $\delta$ , of each parameter. Calculated support is most sensitive to density depletion.

705       To develop greater statistical insight, we performed a Monte-Carlo error analysis. One million  
 706       calculations of isostatic support in response to thinning the lithosphere by 1 km, and unit adjustments  
 707       to all other parameters, were performed. All parameters were varied within specified ranges  
 708       and have well-defined (mostly normal) distributions (Figure 9). Crustal thickness was varied such  
 709       that the mean and variance reflected values observed within the North American Western Interior  
 710       (mean = 40 km, standard deviation = 10 km; *Buehler & Shearer*, 2016). Initial lithospheric thickness  
 711       was also assigned a mean of 150 km and standard deviation of 30 km, reflecting the vertical res-  
 712       olution of the SLNAAFS tomography model. The thermal expansion coefficient,  $3.3 \times 10^{-5} \text{ K}^{-1}$ , was  
 713       assigned a 10% standard deviation, which encompasses the predicted range of values as reported by  
 714       *Bouhifd et al.* (1996) and *Katsura et al.* (2009). Similarly, the temperature at the base of the litho-  
 715       sphere, 1200°C, adiabatic gradient, simplified to 4.44°C/km, and reference mantle density, 3.33 Mg  
 716        $\text{m}^{-3}$ , were all assumed to have a standard deviation of 10%. Mantle potential temperature, 1333°C,  
 717       was assigned a standard deviation of 100°C, which encompasses a range of values for ‘standard’ man-  
 718       tle (*Parsons & Sclater*, 1977). Lithospheric density depletion was assigned an exponential distri-  
 719       bution such that 50% of tested densities are between 3.3 and 3.29 Mg  $\text{m}^{-3}$ , 30% are between 3.29  
 720       and 3.27 Mg  $\text{m}^{-3}$ , and 20% are between 3.27 and 3.25 Mg  $\text{m}^{-3}$ . Figure 9 shows uplift following 1  
 721       km of lithospheric thinning; First, all uncertainties were incorporated by varying all parameters si-  
 722       multaneously, shown in Figure 9A, while Figure 9 B–I do the same calculation while holding all vari-  
 723       ables fixed except one.

724       The results show that there is a well-defined peak in predicted support centered at ~24 m per  
 725       km thinning, with a large uncertainty. Most of the uncertainty is a consequence of uncertain back-  
 726       ground mantle potential temperatures, thermal expansion coefficient values, temperatures at the base  
 727       of the lithosphere, and mantle density depletion factors. If the density of lithospheric mantle is known,  
 728       the uncertainty in predicted isostatic support is significantly reduced (see Figure 9). We now explore  
 729       how the histories of uplift inferred from the inventory of uplifted marine rock can be used to assess  
 730       the history of shallow isostatic support. We seek to quantify the roles asthenospheric temperature  
 731       anomalies and changes to lithospheric architecture played in post-Cretaceous uplift of North Amer-  
 732       ica.

**Table 2.** Calculated variance of lithospheric isostatic support,  $\Delta U$ , from a systematic sweep of modified parameter values (from reference values indicated in second column). Variance of parameter values,  $\delta$ , are given in third column. Parameters: crustal thickness ( $t_{cc}$ , km), lithospheric density depletion factor ( $d$ ), geothermal gradient ( $dT/dz$ , °C  $\text{km}^{-1}$ ), mantle potential temperature ( $T_p$ , °C), temperature of thermal boundary layer ( $T_{bl}$ , °C). % indicates percentage difference to calculated support for reference lithosphere ( $U = 0.03 \text{ km}$ ). Sensitivity analysis for thinning 200 km-thick lithosphere can be found in the Supplementary Information.

| Parameter | Reference value | $\delta$   | $\Delta U$ (km)          | %     |
|-----------|-----------------|------------|--------------------------|-------|
| $t_{cc}$  | 40              | $\pm 1$    | $1.70 \times 10^{-4}$    | 0.65  |
| $d$       | 0               | $+0.01$    | $-1.0245 \times 10^{-2}$ | -39.3 |
| $dT/dz$   | 0.44            | $\pm 0.01$ | $5.9 \times 10^{-5}$     | 0.23  |
| $T_p$     | 1333            | $\pm 1$    | $4.7 \times 10^{-5}$     | 0.18  |
| $T_{bl}$  | 100             | $\pm 1$    | $3.2 \times 10^{-5}$     | 0.12  |

## 733 5 Exploring shallow isostatic origins for the history of observed uplift

734 First, we examine the consequences of assuming that lithospheric thinning alone can explain  
 735 observed patterns of uplift. Thermally equilibrated lithospheric thinning requires the thermal bound-  
 736 ary layer (between the lithosphere and convecting mantle) to be present during thinning. In con-  
 737 trast, thermally disequilibrated thinning implies that the thermal boundary layer is removed instan-  
 738 taneously during thinning and replaced by asthenospheric mantle, creating a discontinuity in tem-  
 739 perature across the LAB. We test these two end-member scenarios to place lower and upper bounds  
 740 on calculated uplift. Calculated uplift from thinning of thermally equilibrated and disequilibrated  
 741 lithosphere with initial thicknesses (at 0 uplift) of 150, 200 and 250 km are shown in Figure 10B,  
 742 colored by geographic province (Equation 4). Uplift of the Great Plains and most of the Middle Rocky  
 743 Mountains can be explained by thinning initially thick ( $> 200$  km) lithosphere, while uplift of the  
 744 Colorado Plateau and Basin and Range can be explained by thinning of an originally relatively thin  
 745 ( $< 150$  km) lithosphere.

746 The distribution of calculated lithospheric thicknesses are broadly bimodal (see histogram atop  
 747 Figure 10B). Thus, to simplify our approach, we estimate uplift from lithospheric thinning for only  
 748 these two modes. We do so by back-projecting the centroids of lithospheric thickness-uplift pairs along  
 749 equilibrium and disequilibrium lithospheric thinning trajectories (Figure 10C: solid, dashed gray and  
 750 black lines). The centroids were identified using a *k-means* algorithm (see Supporting Figure S10).  
 751 Figure 10C-D shows the results of the *k-means* clustering algorithm. The number of clusters is cho-  
 752 sen *a priori* by calculating the total within-cluster sum of squared distances (WCSS; see Support-  
 753 ing Information). The first centroid is (60 km, 1.8 km) and contains localities mostly within the Col-  
 754 orado Plateau, Basin and Range, and parts of the Middle and Northern Rocky Mountains. The sec-  
 755 ond centroid is (170 km, 1.1 km), at the center of a cluster encompassing localities from the Cana-  
 756 dian shield and Interior Lowlands. Calculated initial lithospheric thicknesses for the two clusters are  
 757 130 km and 200 km. This result can be explained by thinning of lithosphere beneath the Colorado  
 758 Plateau and Basin and Range from 130 km to 80–70 km. The second cluster contains loci atop litho-  
 759 sphere that progressively thins to the West by as much as 100 km. These results indicate that the  
 760 tilting of the Great Plains, with highest uplift in the Southern and Middle Rocky Mountains, can  
 761 be explained by thinning of lithosphere that was initially  $\sim 200$  km thick.

762 Secondly, we explore an alternative explanation in which lithosphere with different densities  
 763 are thinned. Estimates of lithospheric mantle density from gravity modeling suggests that cratonic  
 764 lithosphere, present beneath the eastern region of our study area, has a density depleted by 30–70  
 765 kg m<sup>-3</sup> (Mooney & Kaban, 2010). Lamb et al. (2020) proposed that the lithosphere here is depleted  
 766 by 20–40 kg m<sup>-3</sup> compared to the asthenospheric mantle. Figure 10D shows thinning trajectories  
 767 for a lithosphere that is initially 225 km thick (e.g., the modern Canadian Shield). It shows results  
 768 for different assumed reductions in density. A useful rule of thumb is that a 1% reduction lowers den-  
 769 sity by  $\approx 36$  kg m<sup>-3</sup>. Assuming that lithospheric mantle densities were 1–2% depleted (prior to thin-  
 770 ning) implies that up to 150 km of thinning, from an initial thickness of 250 km (across the entire  
 771 domain), would be required to explain observed patterns of uplift. That would constitute a major  
 772 geological event that could be tested in the future using independent observations of, for example,  
 773 heat flow and xenolith-derived paleo-lithospheric thicknesses, and more granular uplift histories.

## 774 6 Discussion

775 There now exists a considerable body of quantitative paleogeographic, uplift and subsidence  
 776 observations with which surface deflections predicted by geodynamic models of the mantle can be  
 777 tested (e.g., PBDB, MacroStrat; Figures 1–3). In this study, we augmented marine fossil assemblages  
 778 recorded in the PBDB with stratigraphic information to test the timing, amplitude and distribution  
 779 of dynamic topography of Western North America predicted by the models presented by Müller *et*  
 780 *al.* (2018).

781 Their Model M1 does not explain post-Cretaceous net uplift (it is lower by up to a factor of  
 782 2; Figure 5A). It does however broadly predict paleo-water depths that are consistent with estimates  
 783 from the fossil record (Figure 5B). In contrast, models M2–M4 broadly reproduce amplitudes of net

784 post-Cretaceous uplift (Figure 5C), but do not explain observed patterns of Cretaceous paleo-bathymetry.  
 785 In particular, predicted dynamic drawdown implies a much deeper depth for the Western Interior  
 786 Seaway than its fossil assemblages indicate (e.g. Figure 5D). We note that Müller *et al.* (2018)'s pre-  
 787 ferred model is M7, since it yields realistic continental flooding histories. However, the model ex-  
 788 plicitly suppresses plume formation, which probably reduces similarity to actual mantle convection.  
 789 We note that calculated net dynamic topography in Model 7 is up to a factor of 3 lower than ob-  
 790 served net uplift. Similarly, these models do not explain subsidence histories of basins in the West-  
 791 ern Interior inferred by backstripping stratigraphy (Figure 6). As Müller *et al.* (2018) point out, an  
 792 obvious source of these discrepancies is the lack of contributions to topographic support in these mod-  
 793 els from the uppermost few hundred kilometers. We addressed this issue as follows.

794 Recent shear wave tomographic models were used to estimate lithospheric and asthenospheric  
 795 temperatures, and thence structure (Figures 7–10). This information was combined with simple iso-  
 796 static calculations to assess whether shallow isostatic contributions can explain observed patterns  
 797 of net uplift. Heating shallow asthenospheric mantle alone is unlikely to be sufficient for explain-  
 798 ing observed net uplift. Maximum amplitudes predicted from heating are too low for reasonable pa-  
 799 rameter values (Figure 10A). In contrast, thinning lithospheric mantle (whether depleted or of vari-  
 800 able initial thickness) can, on its own explain, observed patterns of uplift (Figure 10C–D). This pro-  
 801 posed lithospheric thickness evolution is independently supported by petrological modeling of eclog-  
 802 ite xenoliths from the Colorado Plateau, which suggests that up to 80 km of shear-driven removal  
 803 of subcontinental lithospheric mantle occurred between Cretaceous and Eocene times, from an ini-  
 804 tial lithospheric thickness of 200 km to 120–130 km (*Hernández-Uribe & Palin*, 2019). In addition,  
 805 petrological analysis of garnet inclusions in peridotite xenoliths of the same region suggest an ad-  
 806 dditional ~ 50 km of lithospheric thinning, from ~130 km to ~ 80 km, from Eocene to present (*Hunter*  
 807 & *Smith*, 1981; *Ritter & Smith*, 1996). These results are also consistent with histories of sub-lithospheric  
 808 support of Western North America inferred from melt histories of mafic rocks in the region (e.g., *Ball*  
 809 *et al.*, 2021).

810 Figure 11 demonstrates an attempt to reconcile predicted contributions to net uplift of West-  
 811 ern North America. They show the ‘targets’, i.e., net uplift estimated using fossil assemblages and  
 812 associated corrections for paleo-water depth and sea level. Also shown are estimated contributions  
 813 to net uplift from the three sources considered in this paper. First, contributions from the deep man-  
 814 ttle are extracted from Müller *et al.* (2018)'s Model M5. Secondly, isostatic asthenospheric support  
 815 is estimated from excess temperatures calculated using shear wave tomography (Figure 7–8; Equa-  
 816 tion 3). Finally, the residual is attributed to lithospheric thinning, which can be compared to Fig-  
 817 ure 10. The two examples shown include a locality from the Book Cliffs in Western North Amer-  
 818 ica and from eastern Iowa on the Great Plains. These results emphasize the importance of constrain-  
 819 ing lithospheric thicknesses and densities for determining the history of net uplift and thus for us-  
 820 ing such observations to determine the history of mantle convection.

821 We finish by noting that a variety of alternative approaches to predict dynamic support could  
 822 be tested in future work using the uplift and subsidence histories developed in this paper. For in-  
 823 stance, they could be used to test predictions from analytic solutions of the equations of motion, mod-  
 824 els that assimilate tomographic information, adjoint inverse methodologies, and alternative param-  
 825 eterizations of, for example, plate motion histories, surface boundary conditions, mantle composi-  
 826 tion and viscosity, as well as new approaches for incorporating lithosphere–asthenosphere interac-  
 827 tions into geodynamic simulations (e.g., *Davies et al.*, 2023; *Ghelichkhan et al.*, 2021; *Hayek et al.*,  
 828 2021; *Young et al.*, 2022). Refining knowledge of lithospheric densities and structure is likely to re-  
 829 main a fundamental concern in the quantification of sub-plate support of topography and thus in  
 830 the search for the history of mantle convection.

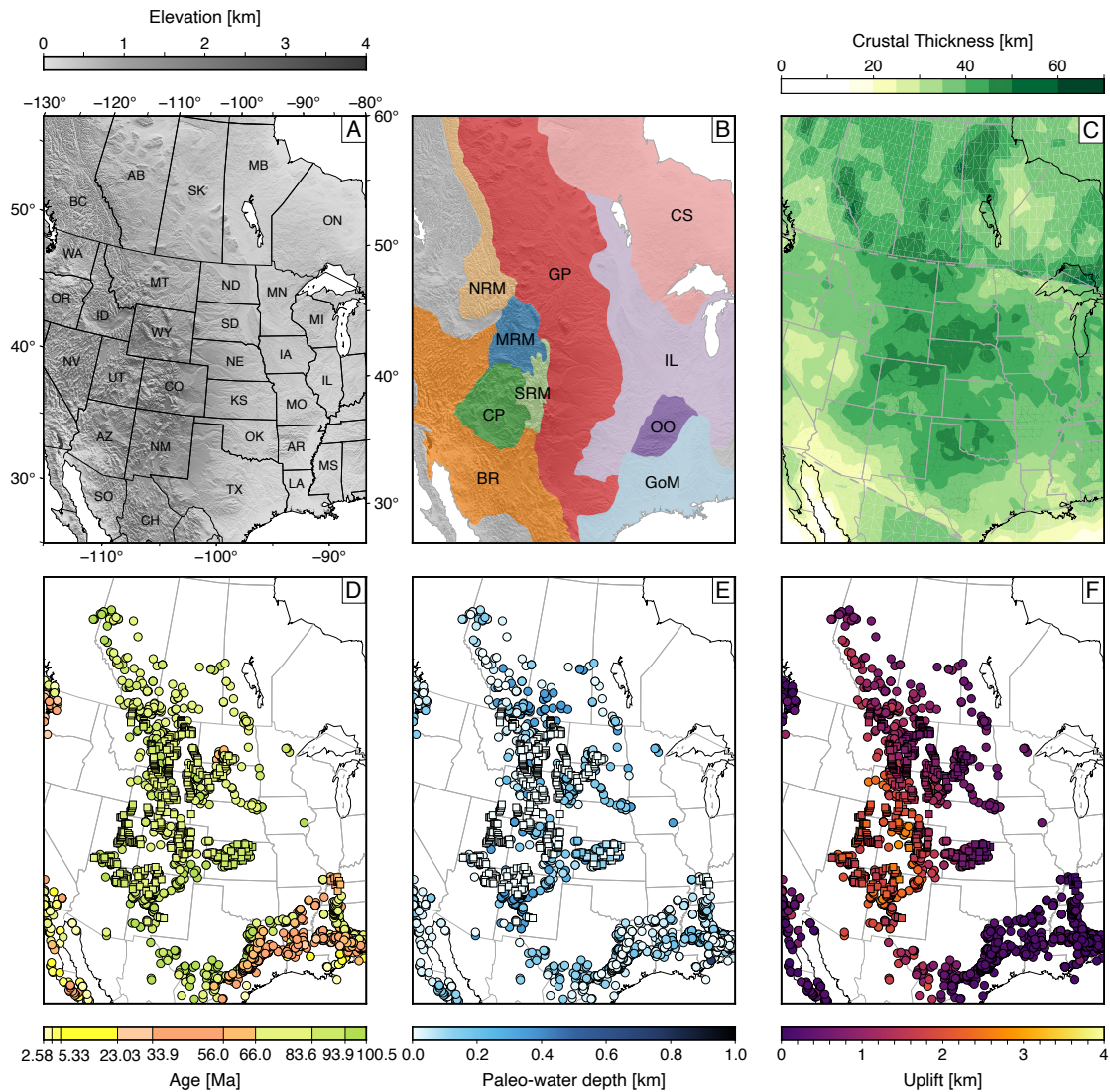
## 831 7 Conclusions

832 Histories of mantle convection and their role in generating vertical motions of Earth surface  
 833 are of general interest. That a considerable body of mantle convection simulations predict differing  
 834 surface deflection histories indicates that identifying optimal models using independent geologic ob-  
 835 servations is likely to be a fruitful endeavor. In this paper we combine digital inventories of pale-

836 obiological data with stratigraphic information to explore origins of western North American topog-  
837 raphy. We demonstrate that geodynamic simulations that exclude the uppermost few hundred kilo-  
838 meters of the mantle cannot, on their own, reproduce observed patterns of vertical motions. We also  
839 demonstrate that excess asthenospheric temperatures, on their own, are insufficient for explaining  
840 net support of Western North American topography. Since crustal thicknesses across this region ap-  
841 pear to be broadly similar we instead, turn to modification of lithospheric mantle as a source of post-  
842 Cretaceous net uplift. We demonstrate that changes to lithospheric thickness and depletion could  
843 explain observed patterns of uplift, and that this proposed mechanism is consistent with indepen-  
844 dent petrological constraints on lithospheric evolution. These results emphasize the importance of  
845 determining the properties (e.g., densities and structure) of the lithosphere (especially the lithospheric  
846 mantle) and its modification by the convecting mantle if we are to understand how the convecting  
847 mantle impacts surface processes and vice versa.

## 848 8 Open Research

849 All data used in this publication are accessible through online, open-access data repositories.  
850 Dynamic topography models from *Müller et al.* (2018) can be accessed through the open data repos-  
851 itory <https://www.earthbyte.org/global-dynamic-topography-models/>. Database for uplift measure-  
852 ments from paleobiological data, from *Fernandes & Roberts* (2021), can be accessed through the open  
853 data repository <https://doi.org/10.1130/GSAB.S.12939470>. All other datasets used in this research  
854 can be accessed in the following data repository: <https://doi.org/10.5281/zenodo.10212951>.

**Figures**

**Figure 1. Western North America and its surroundings.** (A) Hill-shaded elevation map showing USA, Canadian and Mexican state borders, note two-letter state abbreviations (SRTM+; Becker *et al.*, 2009). (B) Physiographic provinces after Fenneman (1928): CS = Canadian Shield; GP = Great Plains; NRM, MRM, SRM = Northern, Middle and Southern Rocky Mountains; CP = Colorado Plateau; BR = Basin and Range; IL = Interior Lowlands; OO = Ozark and Ouachita Mountains; GoM = Gulf of Mexico Coastal Plain. (C) Crustal thickness from CRUST1 (Laske *et al.*, 2013) and PnUS (Buehler & Shearer, 2016). Dashed gray lines = extent of PnUS model. (D) Location of fossil assemblages from the Paleobiology Database (PBDB; circles) indicating youngest outcropping marine to terrestrial (MTT; squares) stratigraphic transitions (Fernandes *et al.*, 2019; Fernandes & Roberts, 2021). Points are colored by stratigraphic age, using the Gradstein *et al.* (2012) timescale (see Figure S1 for colorblind-friendly version). (E) Interpreted paleo-water depth for each location. (F) Net uplift calculated from fossil and stratigraphic data.

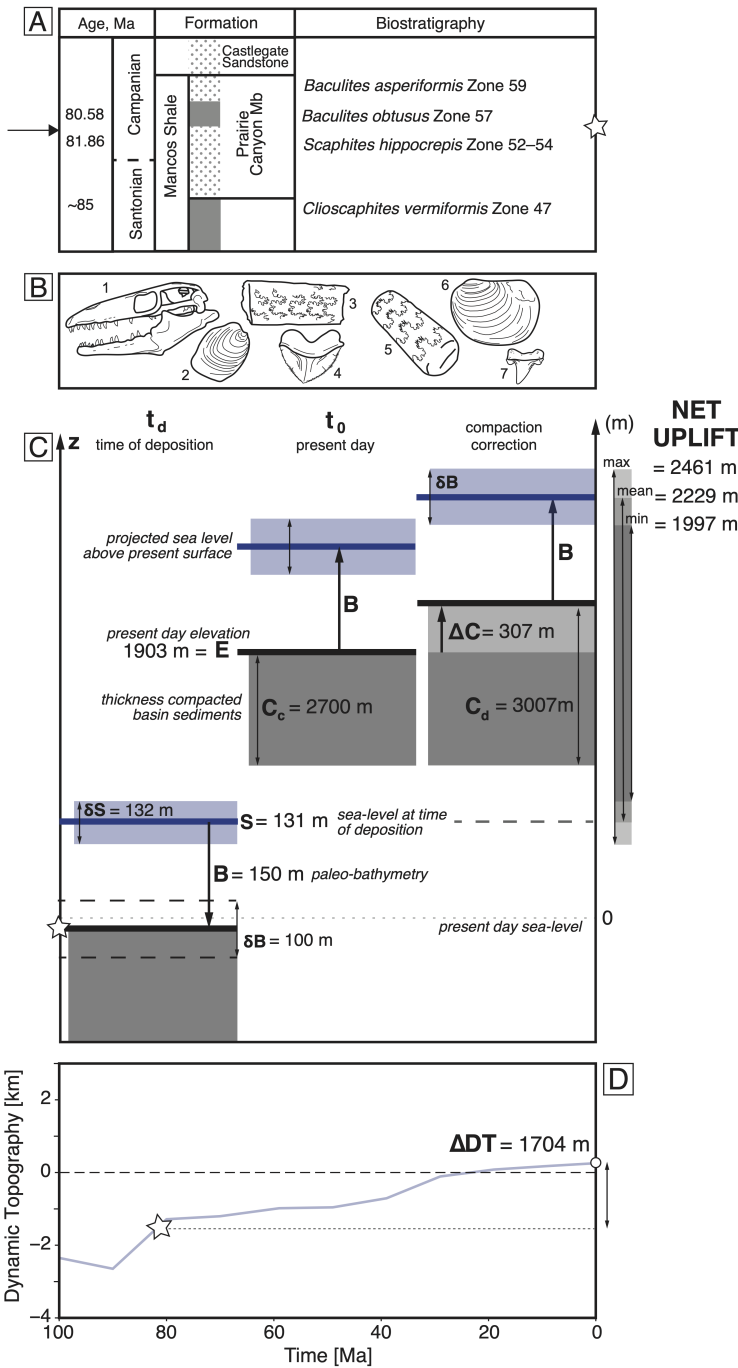


**Figure 2.** Illustration of methodologies used to extract observed and predicted net uplift from geological data and predictions from mantle convection simulations. Loci of the fossil assemblage in the Book Cliffs of Utah and dynamic topographic prediction is labeled ‘3’ in Figure 3. (A) General stratigraphic framework of the Mancos Shale, and associated bio- and chrono-stratigraphic constraints. (B) Fossil assemblage used to constrain the paleo-bathymetry of the Prairie Canyon Member of the Mancos Shale: 1—*Prognathodon*, 2—*Platyceramus cycloides*, 3—*Baculites haresi*, 4—*Squalicorax pristodontus*, 5—*Baculites aquilaensis*, 6—*Innoceramus balticus*, 7—*Cretolamna* (see Fernandes & Roberts, 2021, for more details). (C) Schematic showing net uplift calculation and corrections; see Section 2.2.1 for description of symbols and methodology;  $C_c$  and  $C_d$  = compacted and decompactified stratigraphy. (D) History of dynamic topography from Model M2 of Müller et al. (2018) at the location of the fossil assemblage. The star marks the age of deposition of the fossil assemblage. Net predicted dynamic topography,  $\Delta DT$ , is calculated as the difference between predicted dynamic topography at the time of deposition and the present-day.

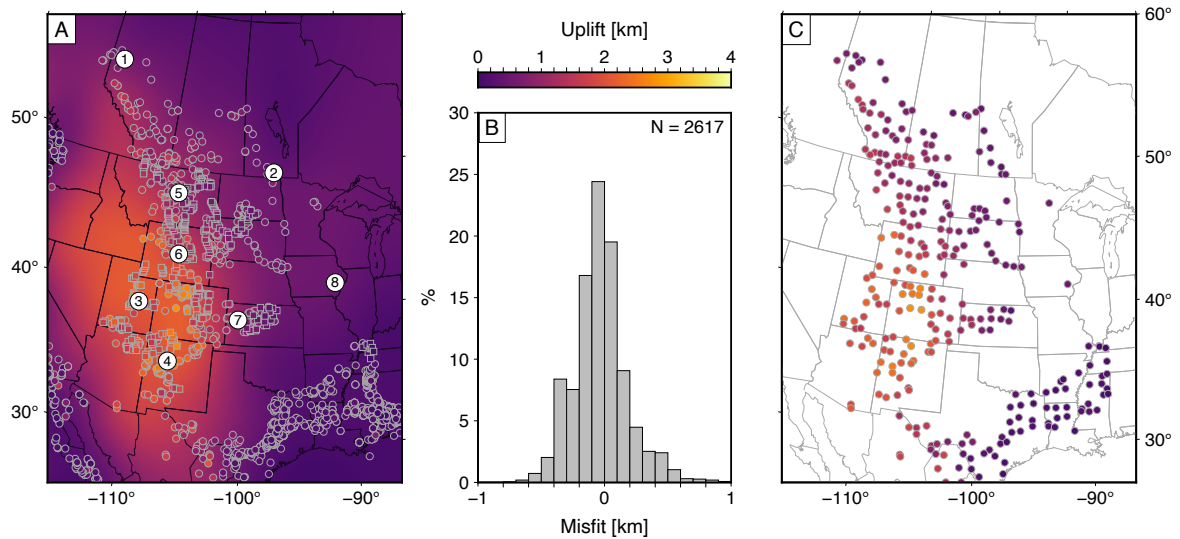


**Figure 3. Large-scale patterns of uplift.** (A) Smooth surface fit to 2617 spot measurements of uplift derived from the PBDB (circles) and marine to terrestrial stratigraphic transitions (squares). Large numbered circles = localities where stratigraphic observations of vertical motion and predicted dynamic topography are shown in Figure 4D and Supplementary Information. Surface was generated using continuous curvature splines and then filtered to remove wavelengths  $< 1000$  km. (B) Difference between uplift estimated from 2617 stratigraphic (PBDB) observations and the smooth surface shown in panel A. (C) Location and mean uplift value for uplift data averaged into  $1^\circ \times 1^\circ$  bins ( $N = 295$ ). Data from the westernmost edge of the North American continent were not included as their uplift history most likely does not reflect a history of mantle-driven vertical motions.

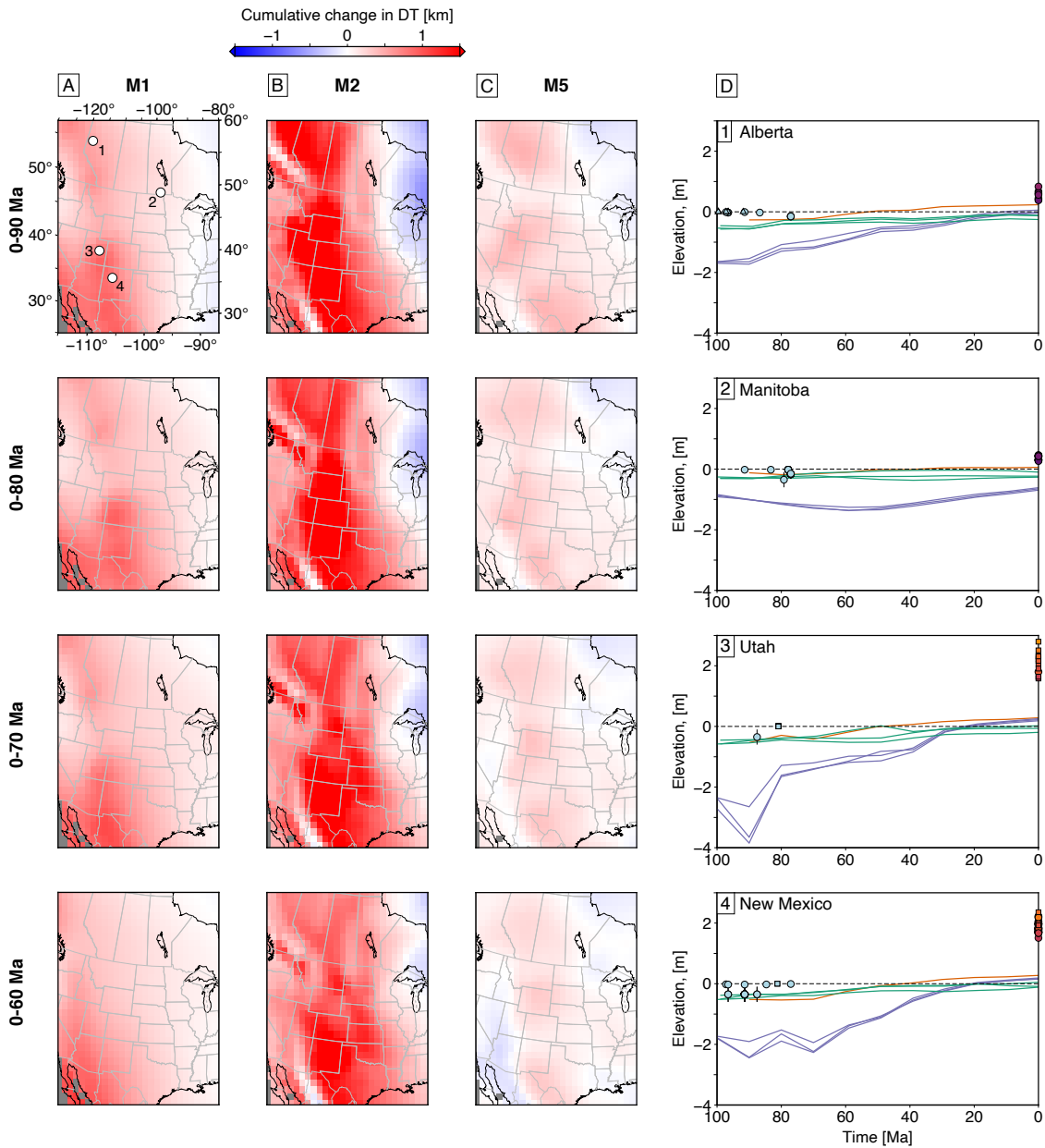


**Figure 4. Comparison of dynamic topography predicted from mantle convection simulations and stratigraphic observations.** Maps show cumulative change in dynamic topography since 90, 80, 70 and 60 Ma predicted by models (A) M1, (B) M2 and (C) M5, which are representative histories produced by families of models generated by Müller *et al.* (2018). Gray lines = state/country boundaries (see Figure 1A). Labeled white circles = locations of stratigraphic constraints and predicted dynamic topography shown in panel D: Alberta (1), Manitoba (2), Utah (3), New Mexico (4). (D) Histories of vertical motion predicted by geodynamic models compared to stratigraphic observations at localities labeled 1–4 in panel A. Orange, purple, green lines = predicted dynamic topography from models M1, M2–M4, M5–M7, respectively (Müller *et al.*, 2018). Circles and squares = stratigraphic observations from PBDB and first recorded terrestrial sediments, respectively, and modern topography; error bars = paleo-water depth uncertainties (colors indicate paleo-water depth, see Figure 1E; see body text for details).

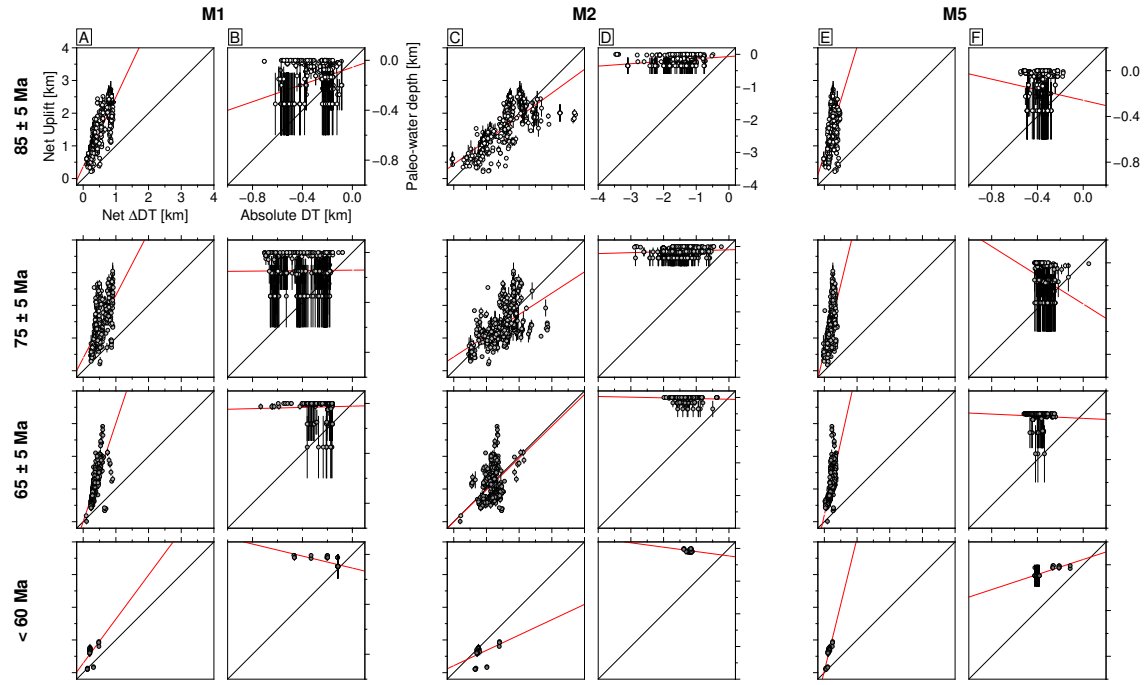


**Figure 5. Comparisons of net (post-deposition) uplift and paleo-water depths from stratigraphic observations to geodynamic model predictions.** (A) Circles = net uplift measured using modern elevation of marine rock compared to net change in predicted dynamic topography (see e.g. Figure 2). Measurements of net uplift are grouped according to age of deposition in  $85 \pm 5$  Ma (top row),  $75 \pm 5$  Ma,  $65 \pm 5$  Ma and  $< 60$  Ma (bottom row) bins (see Figures 1F & 2). Predictions of net dynamic topography ( $\Delta DT$ ) are from model M1 of Müller *et al.* (2018). Measured and predicted motions were averaged in the same  $1^\circ \times 1^\circ$  bins prior to insertion into this panel (see Figure 2); error bars = 1 standard deviation from the mean vertical stratigraphic motions within each  $1 \times 1^\circ$  bin, which includes age and paleo-water depth uncertainties and the range of values in each bin. Black line = 1:1 relationship; red line = best-fit linear least-squares regression. (B) Comparison of predicted absolute elevations from model M1 and paleo-water depth estimates from stratigraphy in labeled age bins. (C-D) Model M2. (E-F) Model M5. See Figure 3.

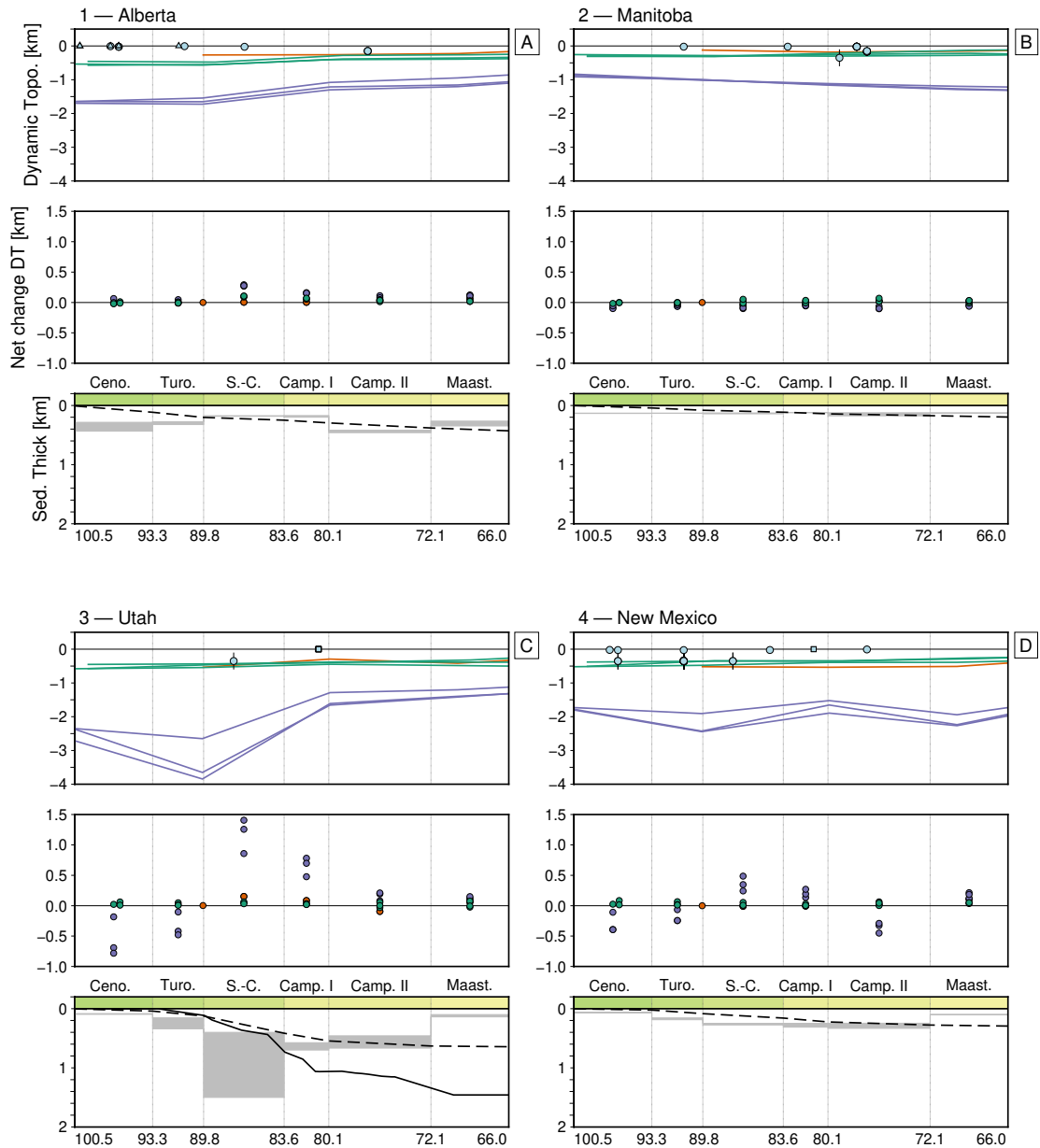


**Figure 6. Comparison of predicted Late Cretaceous dynamic topography and independent subsidence histories.** (A) Observations and predictions from bin (width = 30 km) centered on circle labeled 1 in Figure 2 (Alberta). Top panel: Orange, purple, green lines = predicted dynamic topography from models M1, M2–M4, M5–M7, respectively (*Müller et al., 2018*). Circles = paleo-water depths from biostratigraphic observations; error bars = associated uncertainties, note that in many cases uncertainty is less than symbol size. Triangles = minimum paleo-water depth from marine biostratigraphic constraints where paleo-environment is poorly constrained. Squares = first recorded post-marine terrestrial sediments (*Fernandes et al., 2019*). Vertical lines bound geological stages. Middle panel: Net change in predicted dynamic topography during each stage for the seven mantle convective simulations (colors as for lines in panel A); Ceno = Cenomanian, Turo = Turonian, S-C = Coniacian-Santonian, Camp I & Camp II = Campanian, Maast = Maastrichtian. Negative/positive values indicate predicted net subsidence/uplift. Bottom panel: Black dashed line = subsidence history from backstripping, decompressing and air-loading isopach maps from *Roberts & Kirschbaum (1995)*, see Supplementary Information. Grey bands = sediment thickness within bin for each stage, also from *Roberts & Kirschbaum (1995)*. (B) Manitoba (centered on circle labeled 2 in Figure 2A). (C) Utah (3). (D) New Mexico (4). Black solid line is air-loaded subsidence curve from Well 3 ( $-110.178^\circ$ ,  $39.435^\circ$ ) presented in *Liu et al. (2014)*.

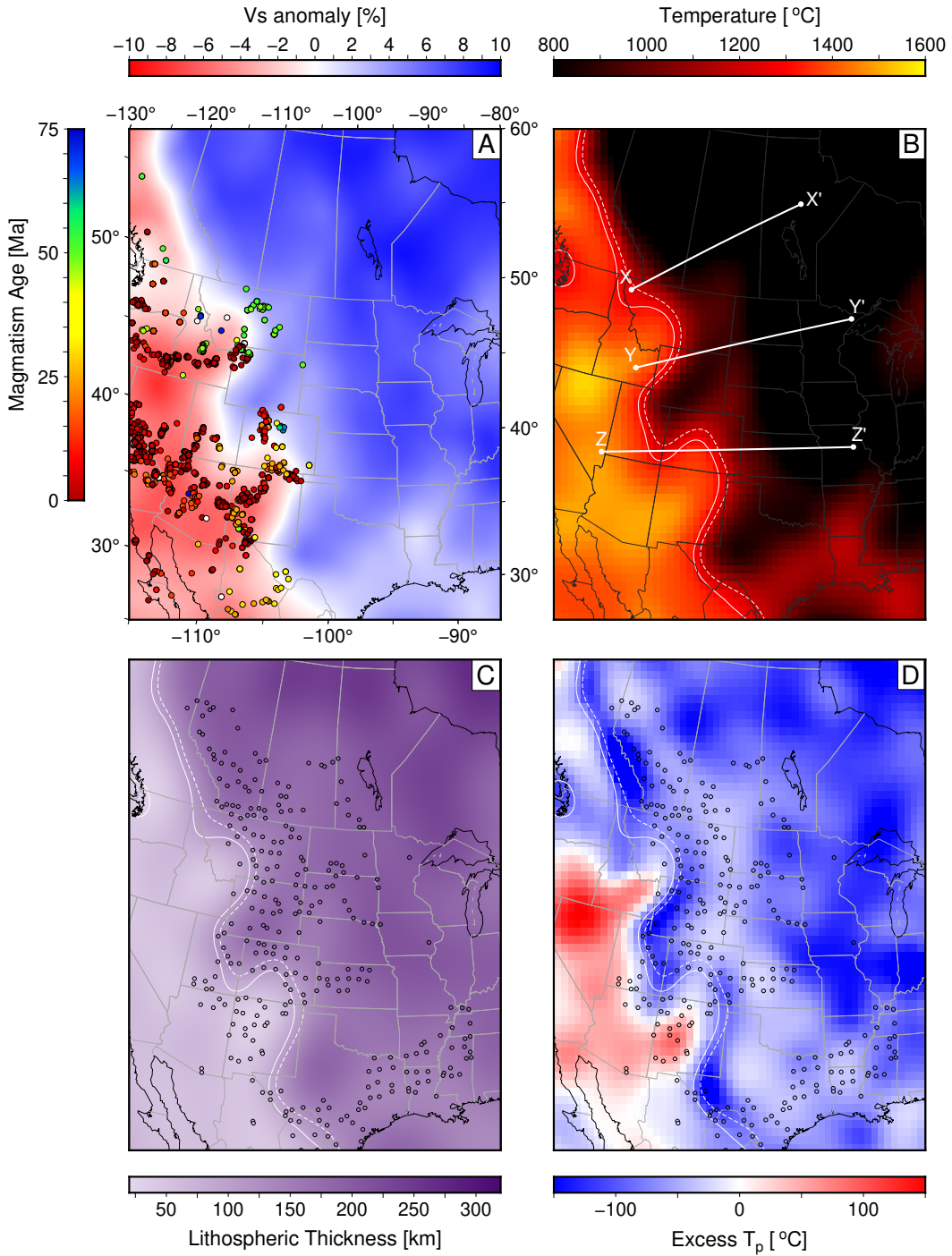


**Figure 7. Shallow mantle geometries, mafic magmatism and uplift constraints.** (A) Shear wave velocity anomaly at 125 km depth from Schaeffer & Lebedev (2013). Circles = magmatism colored by age from NAVDAT database with  $MgO > 4$  wt% (Walker *et al.*, 2006). Gray lines = state/country boundaries. (B) Temperature at 125 km estimated from conversion of Schaeffer & Lebedev (2014)'s shear wave tomography model into temperature (see body text for details). White contours = 1200°C (dashed) and 1300°C (solid) isotherms. Labeled white lines = location of cross sections shown in Figure 8. (C) Lithospheric thickness (defined by 1200°C isotherm), filtered to include spherical harmonic degrees less than  $l = 60$  (wavelengths  $> 660$  km). Black circles = foci of binned ( $1 \times 1^\circ$ ) uplift measurements (see Figure 1). (D) Excess potential temperature of shallowest 100 km beneath the base of the lithosphere. White curves = temperature contours shown in panel B.

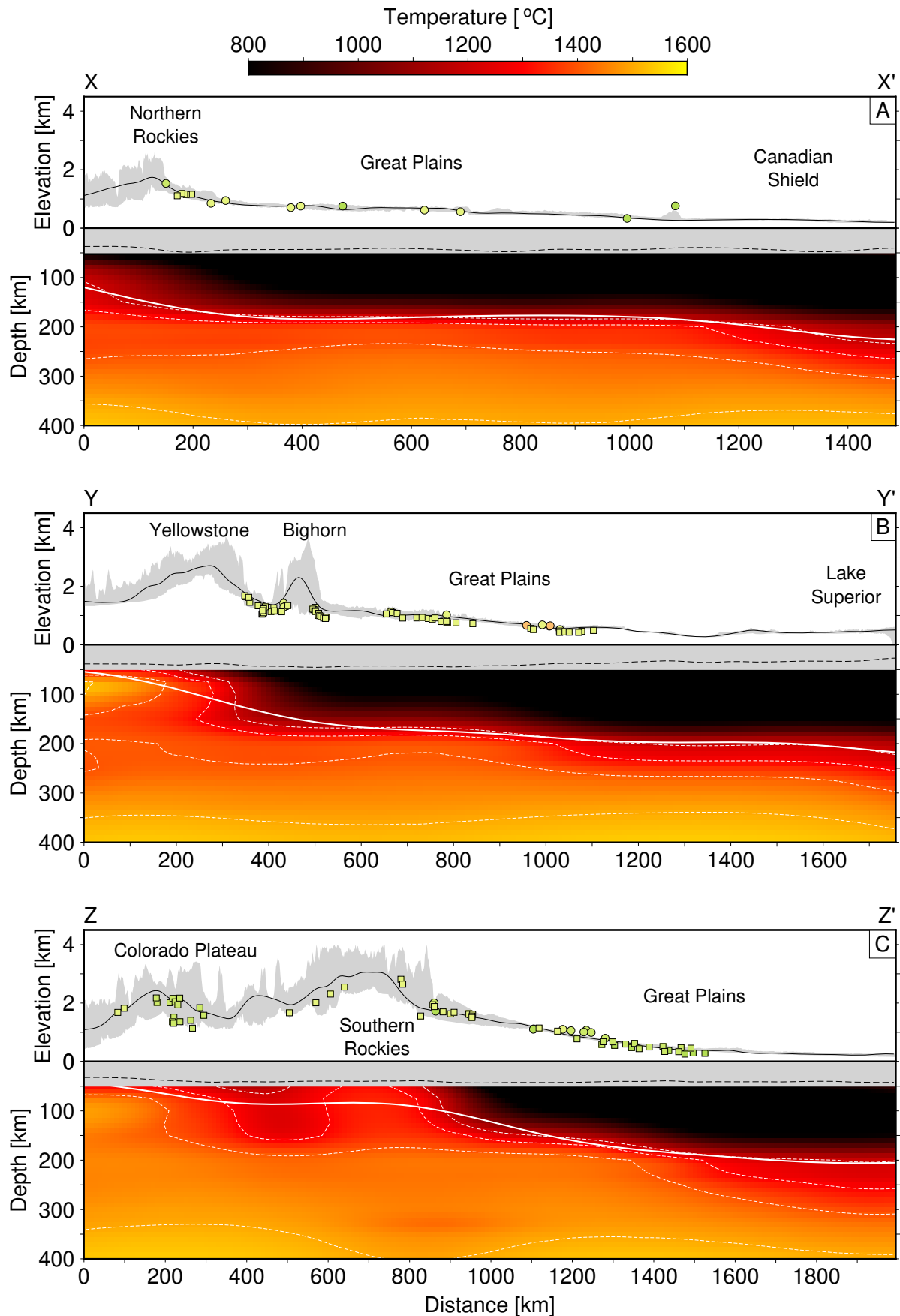


**Figure 8. Cross sections through North American surface observations and calculated shallow mantle temperatures.** (A) Top panel: Black curve = smoothed topography (100 km Gaussian low-pass filter) from Northern Rockies, through the Great Plains to the Canadian Shield (see line labeled X-X' in Figure 6B; (SRTM90: *Jarvis et al.*, 2008). Gray band = maximum and minimum topography within 100 km wide swath. Circles = uplifted marine rocks from PBDB inventory; squares = youngest recorded marine to terrestrial transitional stratigraphy; all samples are from within 100 km wide swath and are colored by age (see Figure 1). Bottom panel: Colors = temperatures calculated by converting a version of *Schaeffer & Lebedev* (2014)'s shear wave model (see body text for details). Thin dotted lines = isotherms in 100°C intervals. Temperatures at depths shallower than 50 km (gray band) are not shown. Black dashed line = crustal thickness from PnUS (*Buehler & Shearer*, 2016). Solid white line = lithosphere-asthenosphere boundary calculated from the 1200°C isotherm smoothed by only including scales less than spherical harmonic degree  $l = 60$  (wavelengths  $> 660$  km). (B-C) Cross sections through Yellowstone to Lake Superior (Y-Y'), and Colorado Plateau to the Great Plains (Z-Z'; see Figure 6B).

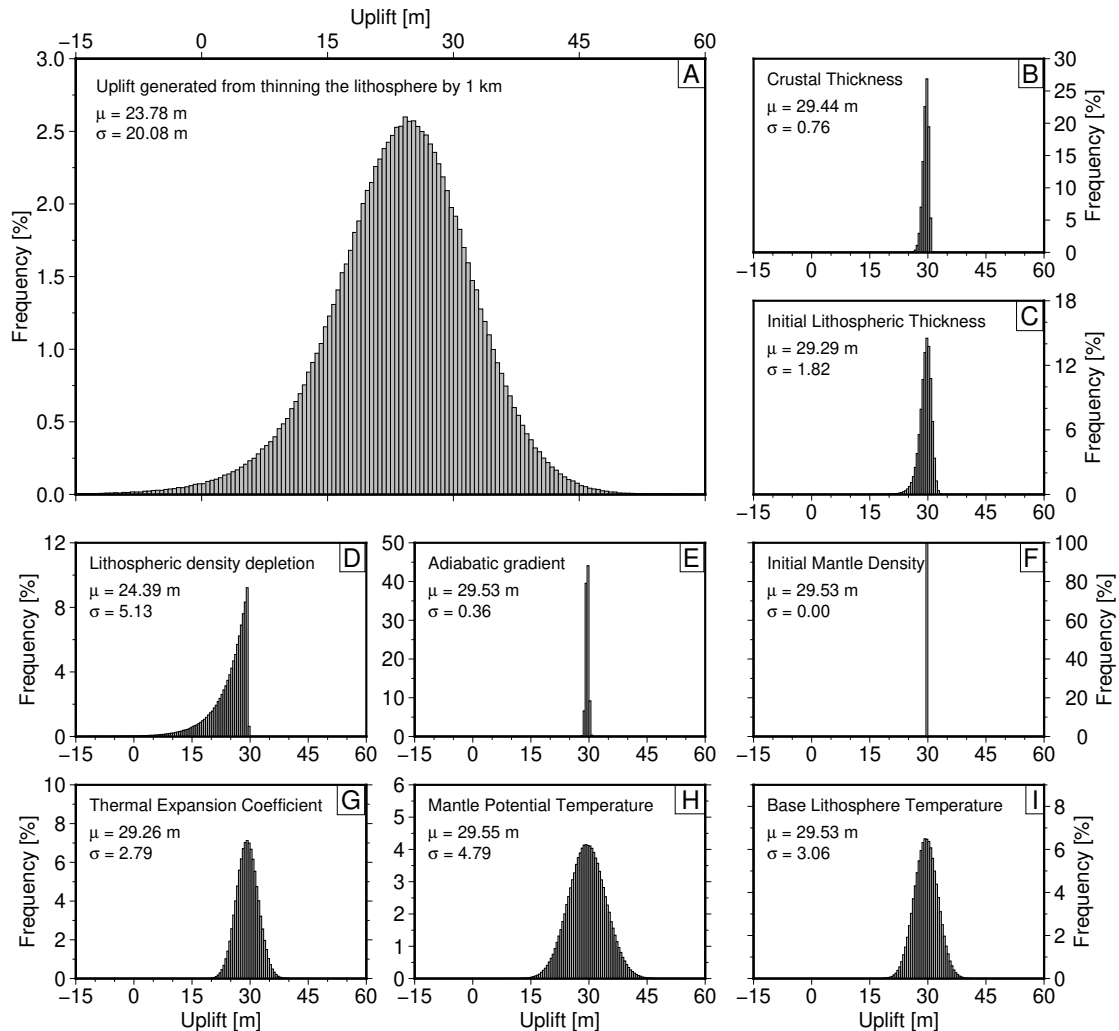


**Figure 9.** Sensitivity of calculated uplift following 1 km of lithospheric thinning (A) Distribution (mean =  $\mu$ , standard deviation =  $\sigma$ ) of calculated isostatic uplift generated by Monte Carlo simulation varying all parameters in Equation 4 simultaneously: crustal thickness, initial lithospheric thickness, lithospheric density depletion, adiabatic gradient, initial mantle density, thermal expansion coefficient, mantle potential temperature and temperature at the base of the lithospheric mantle. Variance of parameters included in this test are indicated in following panels. (B)–(I) Calculated distributions of uplift that arise by holding all parameters fixed except one, annotated in each panel.

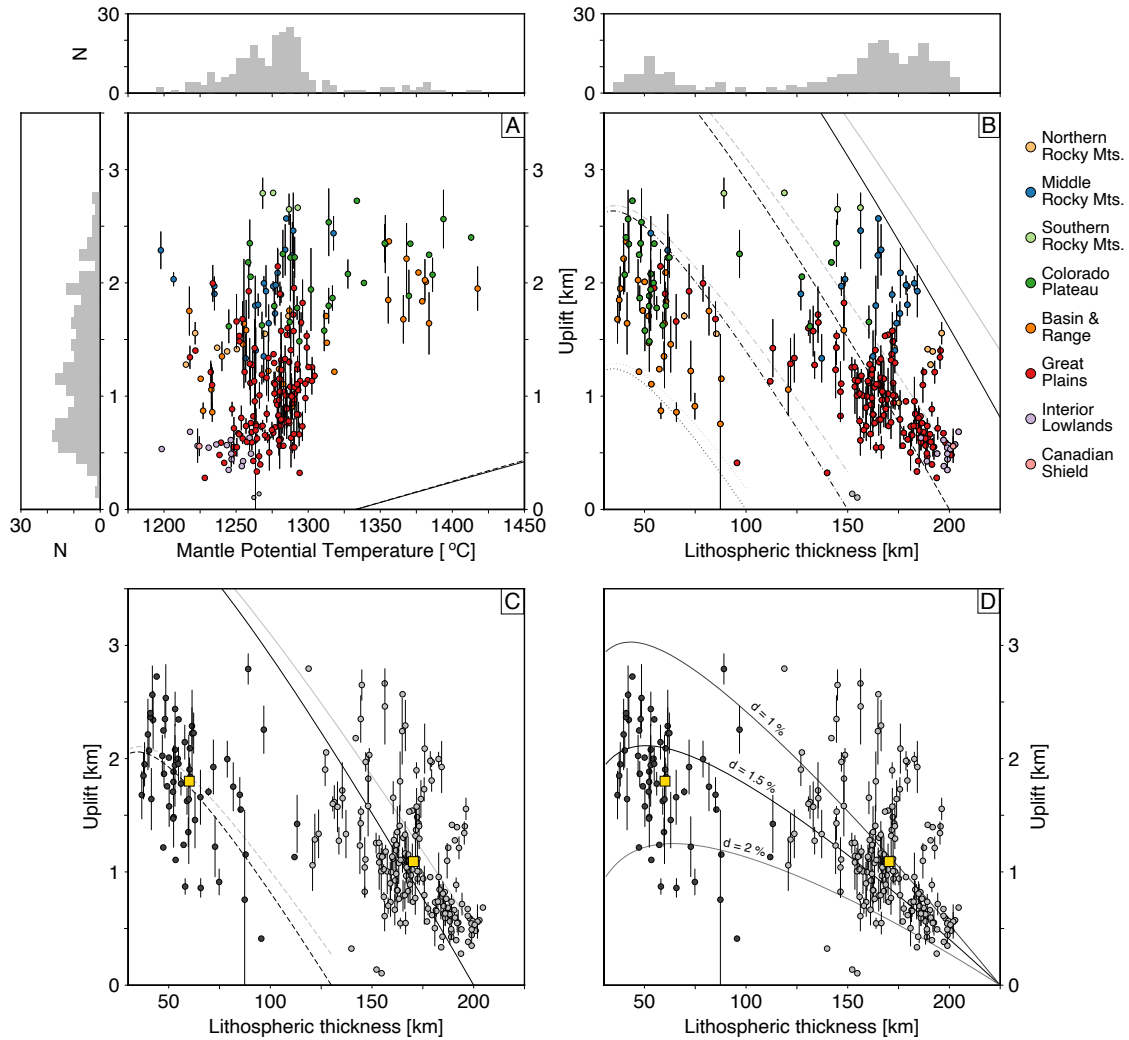


**Figure 10. Assessing the role of lithospheric thinning and asthenospheric temperatures for generating observed uplift.** (A) Uplift measured from stratigraphic observations compared to calculated mean potential temperatures of a 100 km thick asthenospheric channel beneath the base of the lithosphere. Circles = mean values in  $1 \times 1^\circ$  bins; error bars =  $1\sigma$  of uplift measurements in bin. Potential temperatures were extracted from thermal model shown in Figures 6–7 (see body text for details). Circles are colored according to location (see legend); post-Cretaceous uplift data from the Gulf of Mexico coastal plain are not included. Histograms atop and aside main panel show distributions of calculated potential temperatures and uplift measurements, respectively. Lines = predicted isostatic uplift for anomalously warm 100 km (solid) or 200 km (dashed) thick asthenospheric channels (see body text). (B) Uplift measurements in  $1 \times 1^\circ$  bins compared to lithospheric thickness estimates shown in Figure 6C. Black lines = predicted uplift for thermally equilibrated thinning of lithosphere with initial thicknesses of 250 (solid), 200 (dashed), 150 (dot-dashed) or 100 (dotted) km. Nearby gray lines are for thinning without thermal equilibration. (C) Uplift as a function of lithospheric thickness, colored by cluster calculated using k-means clustering algorithm. Yellow squares = cluster centroids. Centroid values are consistent with (thermally equilibrated or disequilibrated) thinning of lithosphere with initial thicknesses of 130 km (black and gray dotted lines) or 200 km (black and gray dashed lines). (D) Black lines show thermally equilibrated thinning of lithosphere with initial thickness of 225 km with different degrees of lithospheric density depletion.

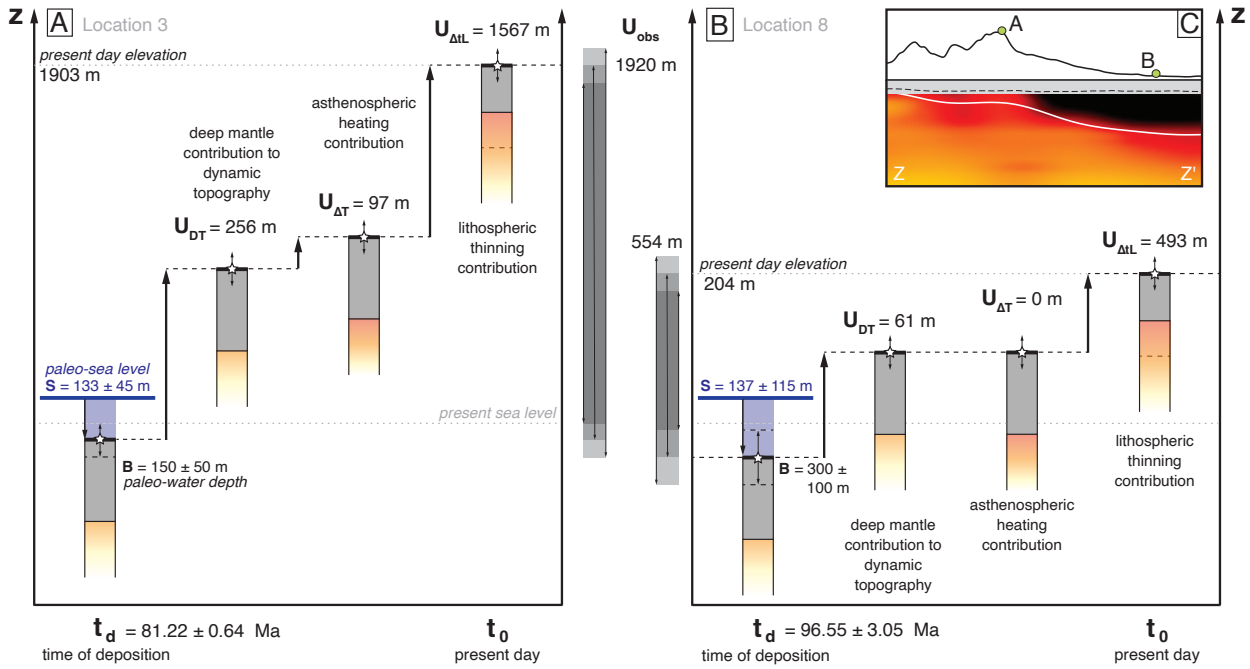


**Figure 11. Reconciling dynamic and isostatic drivers of uplift in the North American Western Interior.** These schematics incorporate dynamic topography predicted by mantle convection simulations (Model M5; Figure 4), and estimated additional asthenospheric heating and lithospheric thinning required to generate observed uplift (see Figure 10 and body text for details). (A) Uplift of the Book Cliffs (Location 3: Figures 2 & 3). Note that the lithospheric thinning required to match observed uplift is significantly less if predictions from models M2–M4 are considered. (B) Uplift in eastern Iowa (Location 8: Figure 3). (C) Schematic cross section across the study region showing the positions of these examples (see Figure 7B: Z–Z' for location).

856 **References**

- Afonso, J.C., Moorkamp, M. and Fullea, J. (2016). Imaging the Lithosphere and Upper Mantle  
in Moorkamp, M., Lelièvre, P.G., Linde, N., and Khan, A. (eds.) *Integrated Imaging of the Earth; Geophysical Monograph Series*. doi: 10.1002/9781118929063.ch10.
- Athy, L.F. (1930). Density, porosity, and compaction of sedimentary rocks. *AAPG Bulletin*, 141, 1-24, doi:10.1306/3D93289E-16B1-11D7-8645000102C1865D.
- Audet, P. (2014). Toward mapping the effective elastic thickness of planetary lithospheres from a spherical wavelet analysis of gravity and topography. *Physics of the Earth and Planetary Interiors*, 226, 48-82, doi:10.1016/j.pepi.2013.09.011.
- Austermann, J., Pollard, D., Mitrovica, J.X., Moucha, R., Forte, A.M., DeConto, R.M., Rowley, D.B. and Raymo, M.E. (2015). The impact of dynamic topography change on Antarctic ice sheet stability during the mid-Pliocene warm period. *Geology*, 43(10), 927-930, doi:10.1130/G36988.1.
- Austermann, J., Mitrovica, J.X., Huybers, P. and Rovere, A. (2017). Detection of a dynamic topography signal in last interglacial sea-level records. *Science Advances*, 3(7), p.e1700457, doi:10.1126/sciadv.1700457.
- Ball, P. W., White, N. J., Maclennan, J. and Stephenson, S. N. (2021). Global influence of mantle temperature and plate thickness on intraplate volcanism. *Nat. Commun.*, 12(2045), doi:10.1038/s41467-021-22323-9.
- Barnett-Moore, N., Hassan, R., Müller, R. D., Williams, S. E., and Flament, N. (2017). Dynamic topography and eustasy controlled the paleogeographic evolution of northern Africa since the mid-Cretaceous. *Tectonics*, 36(5), 929-944, doi:10.1002/2016TC004280.
- Becker, J.J., Sandwell, D.T., Smith, W.H.F., Braud, J., Binder, B., Depner, J., Fabre, D., Factor, J., Ingalls, S., Kim, S-H., Ladner, R., Marks, K., Nelson, S., Pharaoh, A., Sharman, G., Trimmer, R., vonRosenburg, J., Wallace, G., and Weatherall, P. (2009). Global Bathymetry and Elevation Data at 30 Arc Seconds Resolution: SRTM30\_PLUS. revised for *Marine Geodesy*, 32(4), 355-371, doi:10.1080/01490410903297766.
- Bassin, P., Guillocheau, F., Robin, C., Braun, J., Bauer, H., and Schroetter, J.-M. (2017). Quantification of vertical movement of low elevation topography combining a new compilation of global sea-level curves and scattered marine deposits (Armorican Massif, western France). *Earth and Planetary Science Letters*, 470, 25-36, doi:10.1016/j.epsl.2017.04.018.
- Blum, M., and Pecha, M. (2014). Mid-Cretaceous to Paleocene North American drainage reorganization from detrital zircons. *Geology*, 42(7), 607-610, doi:10.1130/G35513.1.
- Bond, G. (1976). Evidence for continental subsidence in North America during the Late Cretaceous global submergence. *Geology*, 4, 557-560, doi:10.1130/0091-7613(1976)4<557:EFCSIN>2.0.CO;2.
- Bouhifd, M. A., Andrault, D., Fiquet, G., and Richet, P. (1996). Thermal expansion of forsterite up to the melting point. *Geophysical Research Letters*, 23(10), 1143-1146, doi:10.1029/96GL01118.
- Buehler J.S. and Shearer, P.M. (2016). Uppermost mantle seismic velocity structure beneath USArray. *Journal of Geophysical Research*, 121, doi:10.1002/2016JB013265.
- Bunge, H. P., and Baumgardner, J. R. (1995). Mantle convection modeling on parallel virtual machines. *Computers in physics*, 9(2), 207-215, doi:10.1063/1.168525.
- Celli, N. L., Lebedev, S., Schaeffer, A. J., and Gaina, C. (2020). African cratonic lithosphere carved by mantle plumes. *Nature communications*, 11(1), 1-10, doi:10.1038/s41467-019-13871-2.
- Celli, N. L., Lebedev, S., Schaeffer, A. J., Ravenna, M., and Gaina, C. (2020). The upper mantle beneath the South Atlantic Ocean, South America and Africa from waveform tomography with massive data sets. *Geophysical Journal International*, 221(1), 178-204, doi:10.1093/gji/ggz574.
- Chamberlain, C.P., Mix, H.T., Mulch, A., Hren, M.T., Kent-Corson, M.L., Davis, S.J., Horton, T.W., and Graham, S.A. (2012). The Cenozoic climatic and topographic evolution of the western north American Cordillera. *American Journal of Science*, 312(2), 213-262, doi:10.2475/02.2012.05.

- 910 Cobban, W.A., Walaszczyk, I., Obradovich, J.D., and McKinney, K.C. (2006). A USGS zonal  
 911 table for the Upper Cretaceous Middle Cenomanian–Maastrichtian of the Western Interior of  
 912 the United States based on Ammonites, Inoceramids, and Radiometric ages. *Technical report.*  
 913 Colli, L., Ghelichkhan, S., and Bunge, H.P. (2016). On the ratio of dynamic topography and  
 914 gravity anomalies in a dynamic Earth. *Geophysical Research Letters*, 43(6), 2510-2516,  
 915 doi:10.1002/2016GL067929.  
 916 Conway-Jones, B. W. and White, N. (2022). Paleogene buried landscapes and climatic aberrations  
 917 triggered by mantle plume activity. *Earth and Planetary Science Letters*, 593, 117644,  
 918 doi:10.1016/j.epsl.2022.117644.  
 919 Cox, K. G. (1989). The role of mantle plumes in the development of continental drainage patterns.  
 920 *Nature*, 342873-877, doi:10.1038/342873a0.  
 921 Craig, C. H., and McKenzie, D. (1987). Surface deformation, gravity and the geoid from a  
 922 three-dimensional convection model at low Rayleigh numbers. *Earth and Planetary Science  
 923 Letters*, 83(1-4), 123-136, doi:10.1016/0012-821X(87)90056-2.  
 924 Cross, T.A. (1986). Tectonic Controls of Foreland Basin Subsidence and Laramide Style De-  
 925 formation, Western United States, in *Foreland Basins*, P.A. Allen and P. Homewood (eds.),  
 926 doi:10.1002/9781444303810.ch1.  
 927 Cross, T.A., and Piliger, R.H. (1978). Tectonic controls of late Cretaceous sedimentation, west-  
 928 ern interior, USA. *Nature*, 247, 653-657, doi:10.1038/274653a0.  
 929 Crough, S. T. (1983). Hotspot swells. *Annual Review of Earth and Planetary Sciences*, 11, 165-  
 930 93.  
 931 Czarnota, K., Roberts, G. G., White, N. J. and Fishwick, S. (2014). Spatial and temporal pat-  
 932 terns of Australian dynamic topography from River Profile Modeling. *Journal of Geophysical  
 933 Research: Solid Earth*, 119(2), 1384-1424, doi:10.1002/2013JB010436.  
 934 Davies, D. R., Ghelichkhan, S., Hoggard, M. J., Valentine, A. P., and Richards, F. D. (2023).  
 935 Observations and models of dynamic topography: Current status and future directions. *Dy-  
 936 namics of Plate Tectonics and Mantle Convection*, 223-269, doi:10.1016/B978-0-323-85733-  
 937 8.00017-2.  
 938 DeCelles, P. G. (1994). Late Cretaceous-Paleocene synorogenic sedimentation and kinematic his-  
 939 tory of the Sevier thrust belt, northeast Utah and southwest Wyoming. *GSA Bulletin*, 106(1),  
 940 32-56, doi:10.1130/0016-7606(1994)106<0032:LCPSSA>2.3.CO;2.  
 941 DeCelles, P. G. (2004). Late Jurassic to Eocene evolution of the Cordilleran thrust belt and  
 942 foreland basin system, Western U.S.A.. *American Journal of Science*, 304 (February), 105-168,  
 943 doi:10.2475/ajs.304.2.105.  
 944 Dickinson, W.R. (2004). Evolution of the North American Cordillera. *Annual Review of Earth  
 945 and Planetary Science*, 32(1), 13-45, doi:10.1146/annurev.earth.32.101802.120257.  
 946 Dickinson, W. R., Klute, M. A., Hayes, M. J., Janecke, S. U., Lundin, E. R., McKittrick, M.  
 947 A., and Olivares, M. D. (1988). Paleogeographic and paleotectonic setting of Laramide sed-  
 948 imimentary basins in the central Rocky Mountain region. *GSA Bulletin*, 100(7), 1023-1039,  
 949 doi:10.1130/0016-7606(1988)100<1023:PAPSOL>2.3.CO;2.  
 950 Ding, X., Dávila, F. M., and Lithgow-Bertelloni, C. (2023). Mechanisms of subsidence and up-  
 951 lift of Southern Patagonia and offshore basins during slab window formation. *Geochemistry,  
 952 Geophysics, Geosystems*, 24(5), e2022GC010844, doi:10.1029/2022GC010844.  
 953 Faccenna, C., Glišović, P., Forte, A., Becker, T. W., Garzanti, E., Sembroni, A. and Gvirtzman,  
 954 Z. (2019). Role of dynamic topography in sustaining the Nile River over 30 million years.  
 955 *Nature Geoscience*, 12(12), 1012-1017, doi:10.1038/s41561-019-0472-x.  
 956 Fenneman, N. (1928). Physiographic Divisions of the United States. *Annals of the Association  
 957 of American Geographers*, 18(4), 261-353, doi:10.2307/2560726.  
 958 Fernandes, V.M., Roberts, G.G., White, N.J., and Whittaker, A.C. (2019). Continental-Scale  
 959 Landscape Evolution: A History of North American Topography. *Journal of Geophysical  
 960 Research: Earth Surface*, 124, 2689-2722, doi:10.1029/2018JF004979.  
 961 Fernandes, V.M., and Roberts, G.G. (2021). Cretaceous to Recent Net Continental Uplift from  
 962 Paleobiological Data: Insights into Sub-Plate Support. *Geological Society of America Bulletin*,  
 963 133(5-6), 1217-1236, doi:10.1130/B35739.1.

- 964 Fernandes, V. M., and Roberts, G. G. (2021). Supplemental Material: Cretaceous  
 965 to Recent net continental uplift from paleobiological data: Insights into sub-  
 966 plate support. [Data set]. *Geological Society of America*. Journal contribution.  
 967 <https://doi.org/10.1130/GSAB.S.12939470.v1>
- 968 Fernandes, V. M. (2023). Open Research Datasets - Testing Mantle Convection Simulations  
 969 with Paleobiology and Other Stratigraphic Observations: Examples from Western North  
 970 America [Data set]. *Zenodo*. <https://doi.org/10.5281/zenodo.10212951>
- 971 Fitton, J.G., James, D., and Leeman, W.P. (1991). Basic magmatism associated with Late  
 972 Cenozoic extension in the western United States: Compositional variations in space and time.  
 973 *Journal of Geophysical Research*, 96(B8), 13693, doi:10.1029/91JB00372.
- 974 Flament, N., Gurnis, M. and Müller, R.D. (2013). A review of observations and models of dy-  
 975 namic topography. *Lithosphere*, 52, 189-210, doi:10.1130/L245.1.
- 976 Flament, N., Williams, S., Müller, R., Gurnis, M. & Bower, D. (2017). Origin and evolution  
 977 of the deep thermochemical structure beneath Eurasia. *Nature Communications*, 8, 14164,  
 978 doi:10.1038/ncomms14164.
- 979 Flowers, R.M., Wernicke, B.P., and Farley, K.A. (2008). Unroofing, incision, and uplift history  
 980 of the southwestern Colorado Plateau from apatite (U-Th)/He thermochronometry. *GSA*  
 981 *Bulletin*, 120(5-6), 571-587, doi:10.1130/B26231.1.
- 982 Flowers, R.M., Ault, A.K., Kelley, S.A., Zhang, N., and Zhong, S. (2012). Epeirogeny or eu-  
 983 stasy? Paleozoic-Mesozoic vertical motion of the North American continental interior from  
 984 thermochronometry and implications for mantle dynamics. *Earth and Planetary Science Let-  
 985 ters*, 317-318, 436-445, doi:10.1016/j.epsl.2011.11.015.
- 986 Flowers, R.M., and Farley, K.A. (2012). Apatite  ${}^4\text{He}/{}^3\text{He}$  and (U-Th)/He Evidence for an An-  
 987 cient Grand Canyon. *Science*, 338, 1616-1619, doi:10.1126/science.1229390.
- 988 Forte, A.M., Peltier, W.R., Dziewonski, A.M., and Woodward, R.L. (1993). Dynamic surface  
 989 topography: A new interpretation based upon mantle flow models derived from seismic to-  
 990 mography. *Geophysical Research Letters*, 20(3), 225-228, doi:10.1029/93GL00249.
- 991 Forte, A.M. (2000). Seismic-Geodynamic Constraints on Mantle Flow: Implications for Layered  
 992 Convection, Mantle Viscosity, and Seismic Anisotropy in the Deep Mantle, in Karato, S.I.,  
 993 Forte, A., Liebermann, R., Masters, G., and Stixrude, L. (eds.) *Earth's Deep Interior: Min-  
 994 eral Physics and Tomography From the Atomic to the Global Scale*. American Geophysical  
 995 Union–Geophysical Monograph Series, 117, doi:10.1029/GM117p0003.
- 996 Forte, A.M., Mitrovica, J.X., Moucha, R., Simmons, N.A., and Grand, S.P. (2007). Descent of  
 997 the ancient Farallon slab drives localized mantle flow below the New Madrid seismic zone.  
 998 *Geophysical Research Letters*, 34(4), doi:10.1029/2006GL027895.
- 999 Forte, A.M., Moucha, R., Simmons, N.A., Grand S.P., and Mitrovica, J.X. (2009). Deep-mantle  
 1000 contributions to the surface dynamics of the North American continent. *Tectonophysics*,  
 1001 481(1-4), 3-15, doi:10.1016/j.tecto.2009.06.010.
- 1002 Forte, A.M., Quéré, S., Moucha, R., Simmons, N. A., Grand, S.P., Mitrovica, J.X., and Rowley,  
 1003 D.B. (2010). Joint seismic–geodynamic-mineral physical modelling of African geodynamics:  
 1004 A reconciliation of deep-mantle convection with surface geophysical constraints. *Earth and*  
 1005 *Planetary Science Letters*, 295(3–4), 329-341, doi:10.1016/j.epsl.2010.03.017.
- 1006 Galloway, W.E., Whiteaker, T.L., and Ganey-Curry, P. (2011). History of Cenozoic North  
 1007 American drainage basin evolution, sediment yield, and accumulation in the Gulf of Mex-  
 1008 ico basin. *Geosphere*, 7(4), 938-973, doi:10.1130/GES00647.1.
- 1009 Gani, R.M., Ranson, A., Cross, D.B., Hampson, G.J., Gani, N.D., and Sahoo, H. (2015).  
 1010 Along-strike sequence stratigraphy across the Cretaceous shallow marine to coastal-  
 1011 plain transition, Wasatch Plateau, Utah, U.S.A.. *Sedimentary Geology*, 325, 59-70,  
 1012 doi:10.1016/j.sedgeo.2015.05.003.
- 1013 Ghelichkhan, S., Bunge, H., and Oeser, J. (2021). Global mantle flow retrodictions for the  
 1014 early Cenozoic using an adjoint method: evolving dynamic topographies, deep mantle struc-  
 1015 tures, flow trajectories and sublithospheric stresses. *Geophysical Journal International*, 226,  
 1016 1432–1460. doi:10.1093/gji/ggab108.
- 1017 Gradstein, F.M., Ogg, J.G., Schmitz, M.B., and Ogg, G.M. (eds.) (2012). *The geologic time  
 1018 scale*, Elsevier, Oxford, UK.

- 1019 Gurnis, M. (1988). Large-scale mantle convection and the aggregation and dispersal of supercontinents. *Nature*, 332(6166), 695-699, doi:10.1038/332695a0.
- 1020 Gurnis, M. (1990). Bounds on global dynamic topography from Phanerozoic flooding of continental platforms, *Nature*, 344, 754-756, doi:10.1038/344754a0.
- 1021 Gurnis, M. (1993). Phanerozoic marine inundation of continent driven by dynamic topography above subducting slabs, *Nature*, 364, 590-593, doi:10.1038/364589a0.
- 1022 Gurnis, M., Mitrovica, J.X., Ritsema, J., and van Heijst, H.J. (2000). Constraining mantle density structure using geological evidence of surface uplift rates: The case of the African Superplume. *Geochemistry, Geophysics Geosystems*, 1(7), doi:10.1029/1999GC000035.
- 1023 Gurnis, M., Turner, M., Zahirovic, S., DiCaprio, L., Spasojevic, S., Müller, R., Boyden, J., Setton, M., Manea, V., and Bower, D. (2012). Plate tectonic reconstructions with continuously closing plates, *Computers and Geosciences*, 38, 35-42, doi:10.1016/j.cageo.2011.04.014.
- 1024 Hager, B. H., Clayton, R. W., Richards, M. A., Comer, R. P., and Dziewonski, A. M. (1985). Lower mantle heterogeneity, dynamic topography and the geoid. *Nature*, 313(6003), 541-545, doi:10.1038/313541a0.
- 1025 Hager, B. H., and Richards, M. A. (1989). Long-wavelength variations in Earth's geoid: physical models and dynamical implications. *Philosophical Transactions of the Royal Society of London. Series A, Mathematical and Physical Sciences*, 328(1599), 309-327, doi:10.1098/rsta.1989.0038.
- 1026 Hampson, G.J., (2010). Sediment dispersal and quantitative stratigraphic architecture across an ancient shelf. *Sedimentology*, 57, 96-141, doi:10.1111/j.1365-3091.2009.01093.x.
- 1027 Hartley, R. A., Roberts, G. G., White, N., and Richardson, C. (2011). Transient convective uplift of an ancient buried landscape. *Nature Geoscience*, 4(8), 562-565, doi:10.1038/ngeo1191.
- 1028 Hassan, R., Flament, N., Gurnis, M., Bower, D.J., and Müller, D. (2015). Provenance of plumes in global convection models, *Geochemistry, Geophysics, Geosystems*, 16, 1465-1489.
- 1029 Hayek, J. N., Vilacís, B., Bunge, H.-P., Friedrich, A. M., Carena, S., and Vibe, Y. (2020). Continent-scale Hiatus Maps for the Atlantic Realm and Australia since the Upper Jurassic and links to mantle flow induced dynamic topography, *Proc.R.Soc.A*, 476, 2242, doi:10.1098/rspa.2020.0390.
- 1030 Hayek, J. N., Vilacís, B., Bunge, H.-P., Friedrich, A. M., Carena, S., and Vibe, Y. (2021). Correction: Continent-scale Hiatus Maps for the Atlantic Realm and Australia since the Upper Jurassic and links to mantle flow-induced dynamic topography, *Proc.R.Soc.A*, 477, 2251, doi:10.1098/rspa.2021.0437.
- 1031 Hazzard, J. A., Richards, F. D., Goes, S. D., and Roberts, G. G. (2023). Probabilistic assessment of Antarctic thermomechanical structure: Impacts on ice sheet stability. *Journal of Geophysical Research: Solid Earth*, 128(5), e2023JB026653, doi:10.1029/2023JB026653.
- 1032 Heine, C., Yeo, L.G., and Müller, R.D. (2015). Evaluating global paleoshoreline models for the Cretaceous and Cenozoic. *Australian Journal of Earth Sciences*, 62(3), 275-287, doi:10.1080/08120099.2015.1018321.
- 1033 Hernández-Uribe, D., and Palin, R. M. (2019). Catastrophic shear-removal of subcontinental lithospheric mantle beneath the Colorado Plateau by the subducted Farallon slab. *Scientific Reports*, 9(1), 8153, doi:10.1038/s41598-019-44628-y.
- 1034 Hintze, L., and Kowallis, B. (2009). Geologic history of Utah, *Brigham Young University Geology Studies Special Publication 9*, Brigham Young University, Salt Lake City, UT.
- 1035 Hoggard, M. J., White, N. and Al-Attar, D. (2016). Global dynamic topography observations reveal limited influence of large-scale mantle flow. *Nature Geoscience*, 9, 456-463, doi:10.1038/10.1038/ngeo2709.
- 1036 Hoggard, M. J., Czarnota, K., Richards, F. D., Huston, D. L., Jaques, A. L., and Ghelichkhan, S. (2020). Global distribution of sediment-hosted metals controlled by craton edge stability. *Nature Geoscience*, 13(7), 504-510, doi: 10.1038/s41561-020-0593-2.
- 1037 Hoggard, M., Austermann, J., Randel, C. and Stephenson, S. (2021). Observational Estimates of Dynamic Topography Through Space and Time, in *Mantle Convection and Surface Expressions*, H. Marquardt, M. Ballmer, S. Cottaar and J. Konter (eds.), doi:10.1002/9781119528609.ch15.

- Holdt, M. C., White, N. J., Stephenson, S. N., and Conway-Jones, B. W. (2022). Densely sampled global dynamic topographic observations and their significance. *Journal of Geophysical Research: Solid Earth*, 127(7), e2022JB024391, doi:10.1029/2022JB024391.
- Hunter, W. C., and Smith, D. (1981). Garnet peridotite from Colorado Plateau ultramafic diatremes: hydrates, carbonates, and comparative geothermometry. *Contributions to Mineralogy and Petrology*, 76, 312-320.
- Huntington, K.W., Wernicke, B.P., and Eiler, J.M. (2010). Influence of climate change and uplift on Colorado Plateau paleotemperatures from carbonate clumped isotope thermometry, *Tectonics*, 29(3), 1-19, doi:10.1029/2009TC002449.
- Jarvis, A., H.I. Reuter, A. Nelson, and E. Guevara (2008). Hole-filled SRTM for the globe Version 4, *CGIAR-CSIRO SRTM 90m Database*, <http://srtm.csi.cgiar.org>.
- Johnson, K.R., Nichols, D.J., and Hartman, J.H. (2002). Hell Creek Formation: a 2001 synthesis, *in*, Hartman, J.H., Johnson, K.R., and Nichols, D.J. (eds.), The Hell Creek Formation and the Cretaceous-Tertiary boundary in the northern Great Plains: An integrated continental record of the end of the Cretaceous, *Geological Society of America Special Paper* 361, Boulder, CO., 503-510.
- Katsura, T., Shatskiy, A., Manthilake, M.G.M., Zhai, S., Fukui, H., Yamazaki, D., Matsuzaki, T., Yoneda, A., Ito, E., Kuwata, A., Ueda, A., Nozawa, A., and Funakoshi, K. (2009). Thermal expansion of forsterite at high pressures determined by in situ X-ray diffraction: The adiabatic geotherm in the upper mantle. *Physics of the Earth and Planetary Interiors*, 174(1-4), 86-92, doi:10.1016/j.pepi.2008.08.002.
- Klöcking, M., White, N.J., MacLennan, J., McKenzie, D., and Fitton, J.G. (2018). Quantitative Relationships Between Basalt Geochemistry, Shear Wave Velocity, and Asthenospheric Temperature Beneath Western North America. *Geochemistry, Geophysics, Geosystems*, 19(9), 3376-3404, doi:10.1029/2018GC007559.
- Lamb, S., Moore, J. D., Perez-Gussinye, M., and Stern, T. (2020). Global whole lithosphere isostasy: implications for surface elevations, structure, strength, and densities of the continental lithosphere. *Geochemistry, Geophysics, Geosystems*, 21(10), e2020GC009150, doi:10.1029/2020GC009150.
- Laske, G., Masters, G., Ma, Z., and Pasyanos, M. (2013). Update on CRUST1.0—A 1-degree global model of Earth's crust, *Geophysical Research Abstracts*, 15, 2658, Vienna, Austria: EGU General Assembly.
- Levandowski, W., Jones, C.H., Butcher, L.A., and Mahan, K.H. (2018). Lithospheric density models reveal evidence for Cenozoic uplift of the Colorado Plateau and Great Plains by lower-crustal hydration, *Geosphere*, 14(3), 1-15, doi:10.1130/GES01619.1.
- Li, Z., and Aschoff, J. (2022). Constraining the effects of dynamic topography on the development of Late Cretaceous Cordilleran foreland basin, western United States. *GSA Bulletin*, 134(1-2), 446-462, doi:10.1130/B35838.1.
- Lipp, A. G., and Roberts, G. G. (2021). Scale-dependent flow directions of rivers and the importance of subplate support. *Geophysical Research Letters*, 48(1), e2020GL091107, doi:10.1029/2020GL091107.
- Liu, L., Spasojević, S., and Gurnis, M. (2008). Reconstructing Farallon plate subduction beneath North America back to the Late Cretaceous. *Science*, 322(January), 934-938, doi:10.1126/science.1167110.
- Liu, S., Nummedal, D., and Gurnis, M. (2014). Dynamic versus flexural controls of Late Cretaceous Western Interior Basin, USA. *Earth and Planetary Science Letters*, 389, 221-229, doi:10.1016/j.epsl.2014.01.006.
- Liu, L., and Gurnis, M. (2008). Simultaneous inversion of mantle properties and initial conditions using an adjoint of mantle convection. *Journal of Geophysical Research: Solid Earth*, 113, doi:10.1029/2008JB005594.
- Lodhia, B. H., Roberts, G. G., Fraser, A. J., Fishwick, S., Goes, S., and Jarvis, J. (2018). Continental margin subsidence from shallow mantle convection: Example from West Africa. *Earth and Planetary Science Letters*, 481, 350-361, doi:10.1016/j.epsl.2017.10.024.
- Lynds, R.M., and Slattery, J.S. (2017). Correlation of the Upper Cretaceous strata of Wyoming, *Wyoming State Geological Survey*.

- 1128 McKenzie, D. P., Roberts, J. M., and Weiss, N. O. (1974). Convection in the Earth's  
 1129 mantle: towards a numerical simulation. *Journal of Fluid Mechanics*, 62(3), 465-538,  
 1130 doi:10.1017/S0022112074000784.
- 1131 McKenzie, D., and Jarvis, G. (1980). The conversion of heat into mechanical work by  
 1132 mantle convection. *Journal of Geophysical Research: Solid Earth*, 85(B11), 6093-6096,  
 1133 doi:10.1029/JB085iB11p06093.
- 1134 McKenzie, D. (1978). Some remarks on the development of sedimentary basins. *Earth and Plan-  
 1135 etary Science Letters*, 40(1), 25-32, doi:10.1016/0012-821X(80)90168-5.
- 1136 McKenzie, D., Jackson, J., and Priestley, K. (2005). Thermal structure of oceanic and  
 1137 continental lithosphere. *Earth and Planetary Science Letters*, 233(3-4), 337-349,  
 1138 doi:10.1016/j.epsl.2005.02.005.
- 1139 Menard, H. W. (1969). Elevation and subsidence of oceanic crust. *Earth and Planetary Science  
 1140 Letters*, 6, 4, 275-284, doi:10.1016/0012-821X(69)90168-X.
- 1141 Merewether, E.A., Cobban, W.A., and Obradovich, J.D. (2011). Biostratigraphic Data from  
 1142 Upper Cretaceous Formations—eastern Wyoming, Central Colorado, and Northeastern New  
 1143 Mexico, *U.S. Geological Survey Scientific Investigations Map 3175*, 2 sheets, pamphlet, 10 p.
- 1144 Merewether, E.A., and McKinney, K.C. (2015). Composite biostratigraphic outcrop sections  
 1145 for Cretaceous Formations along a south-trending transect from northwestern Montana to  
 1146 northwestern New Mexico, *USGS, 1258*, 20151, 087.
- 1147 Mitrovica, J.X., Beaumont, C., and Jarvis, G.T. (1989). Tilting of continental interiors by the  
 1148 dynamical effects of subduction, *Tectonics*, 8(5), 1079-1094, doi:10.1029/TC008i005p01079.
- 1149 Mooney, W. D., and Kaban, M. K. (2010). The North American upper mantle: Density,  
 1150 composition, and evolution. *Journal of Geophysical Research: Solid Earth*, 115(B12),  
 1151 doi:10.1029/2010JB000866.
- 1152 Morris, M., Fernandes, V. M., and Roberts, G. G. (2020). Extricating dynamic topography from  
 1153 subsidence patterns: Examples from Eastern North America's passive margin. *Earth and  
 1154 Planetary Science Letters*, 530, 115840, doi:10.1016/j.epsl.2019.115840.
- 1155 Mouha, R., Forte, A. M., Rowley, D. B., Mitrovica, J. X., Simmons, N. A., and Grand, S.  
 1156 P. (2008). Mantle convection and the recent evolution of the Colorado Plateau and the Rio  
 1157 Grande Rift valley. *Geology*, 36(6), 439-442. doi:10.1130/G24577A.1.
- 1158 Mouha, R., Forte, A. M., Mitrovica, J. X., Rowley, D. B., Quéré, S., Simmons, N. A., and  
 1159 Grand, S. P. (2008). Dynamic topography and long-term sea-level variations: There is no such  
 1160 thing as a stable continental platform. *Earth and Planetary Science Letters*, 271(1), 101-108.  
 1161 doi:10.1016/j.epsl.2008.03.056.
- 1162 Müller, R.D., Flament, N., Matthews, K.J., Williams, S.E., and Gurnis, M. (2016a). Formation  
 1163 of Australian continental margin highlands driven by plate–mantle interaction, *Earth and  
 1164 Planetary Science Letters*, 441, 60–70, doi:10.1016/j.epsl.2016.02.025.
- 1165 Müller, R.D., Seton, M., Zahirovic, S., Williams, S.E., Matthews, K.J., Wright, N.M., Shep-  
 1166 hard, G., Maloney, K.T., Barnett-Moore, N., Hosseinpour, M., Bower, D.J., and Cannon,  
 1167 J. (2016b). Ocean basin evolution and global-scale plate reorganization events since Pangea  
 1168 breakup, *Annual Review of Earth and Planetary Sciences*, 44, 107–138, doi:10.1146/annurev-  
 1169 earth-060115-012211.
- 1170 Müller, R.D., Hassan, R., Gurnis, M., Flament, N., and Williams, S.E. (2018). Dynamic topog-  
 1171 raphy of passive continental margins and their hinterlands since the Cretaceous, *Gondwana  
 1172 Research*, 53, 225-251, doi:10.1016/j.gr.2017.04.028.
- 1173 Obradovich, J.D., and Cobban, W.A. (1975). A time-scale for the Late Cretaceous of the West-  
 1174 ern Interior of North America, *Geological Association of Canada Special Paper 13*, 31-54.
- 1175 Parsons, B. and Daly, S. (1983). The relationship between surface topography, gravity anom-  
 1176 alies, and temperature structure of convection. *Journal of Geophysical Research*, 88(B2),  
 1177 1129-1144, doi:10.1029/JB088iB02p01129.
- 1178 Parsons, B., and Sclater, J. G. (1977). An analysis of the variation of ocean floor  
 1179 bathymetry and heat flow with age. *Journal of Geophysical Research*, 82(5), 803-827,  
 1180 doi:10.1093/petrology/29.3.625.
- 1181 Panasyuk, S. V. and Hager, B. H. (2000). Inversion for mantle viscosity profiles constrained by  
 1182 dynamic topography and the geoid, and their estimated errors. *Geophysical Journal Interna-*

- 1183 *tional*, 143(3), 821-836, doi:10.1046/j.0956-540X.2000.01286.x.
- 1184 Pang, M., and Nummedal, D. (1995). Flexural subsidence and basement tectonics of the Cre-  
1185 taceous Western Interior basin, United States. *Geology*, 23(2), 173-176, doi:10.1130/0091-  
1186 7613(1995)023<0173:FSABTO>2.3.CO;2.
- 1187 Pekeris, C. L. (1935). Thermal convection in the interior of the Earth. *Geophysical Journal  
International*, 3, 343-367, doi:10.1111/j.1365-246X.1935.tb01742.x.
- 1188 Richards, M. A., and Hager, B. H. (1984). Geoid anomalies in a dynamic Earth. *Journal of  
Geophysical Research: Solid Earth*, 89(B7), 5987-6002, doi:10.1029/JB089iB07p05987.
- 1189 Richards, F. D., Coulson, S. L., Hoggard, M. J., Austermann, J. A., Dyer, B., and Mitrovica,  
1190 J. X. (2023). Geodynamically corrected Pliocene shoreline elevations in Australia consist-  
1191 ent with midrange projections of Antarctic ice loss. *Science Advances*, 9(46), eadg3035,  
1192 doi:10.1126/sciadv.adg3035.
- 1193 Richards, F.D., Hoggard, M.J., White, N., and Ghelichkhan, S. (2020). Quantifying the rela-  
1194 tionship between short-wavelength dynamic topography and thermomechanical structure of  
1195 the upper mantle using calibrated parameterization of anelasticity. *Journal of Geophysical  
Research: Solid Earth*, 125(9), e2019JB019062, doi:10.1029/2019JB019062.
- 1196 Richards, F., Hoggard, M., Crosby, A., Ghelichkhan, S., and White, N. (2020). Structure and  
1197 dynamics of the oceanic lithosphere-asthenosphere system. *Physics of the Earth and Plane-  
1198 tary Interiors*, 309, 106559, doi:10.1016/j.pepi.2020.106559.
- 1199 Riter, J. C. A., & Smith, D. (1996). Xenolith constraints on the thermal history of  
1200 the mantle below the Colorado Plateau. *Geology*, 24(3), 267-270, doi:10.1130/0091-  
1201 7613(1996)024<0267:XCOTTH>2.3.CO;2.
- 1202 Richards, F. D., Hoggard, M. J., Cowton, L. R., and White, N. J. (2018). Reassessing the ther-  
1203 mal structure of oceanic lithosphere with revised global inventories of basement depths and  
1204 heat flow measurements. *Journal of Geophysical Research: Solid Earth*, 123(10), 9136-9161,  
1205 doi:10.1029/2018JB015998.
- 1206 Roberts, L.N.R., and Kirschbaum, M.A. (1995). Paleogeography and the Late Cretaceous of  
1207 the Western Interior of middle North America; coal distribution and sediment accumulation.  
1208 *USGS Professional Paper 1561*, doi:10.3133/pp1561.
- 1209 Roberts, G. G., Paul, J. D., White, N., and Winterbourne, J. (2012). Temporal and spatial evo-  
1210 lution of dynamic support from river profiles: A framework for Madagascar. *Geochemistry,  
1211 Geophysics, Geosystems*, 13(4), doi:10.1029/2012GC004040.
- 1212 Roberts, G.G., White, N.J., Martin-Brandis, G.L., and Crosby, A.G. (2012a), An uplift his-  
1213 tory of the Colorado Plateau and its surroundings from inverse modeling of longitudinal river  
1214 profiles, *Tectonics*, 31(4), 1-25, doi:10.1029/2012TC003107.a.
- 1215 Roy, M., Jordan, T.H., and Pederson, J.L. (2009). Colorado Plateau magmatism and uplift by  
1216 warming of heterogeneous lithosphere. *Nature*, 459(7249), 978-82, doi:10.1038/nature08052.
- 1217 Rovere, A., Hearty, P. J., Austermann, J., Mitrovica, J. X., Gale, J., Moucha, R., Forte, A.M.  
1218 and Raymo, M.E. (2015). Mid-Pliocene shorelines of the US Atlantic Coastal Plain—An  
1219 improved elevation database with comparison to Earth model predictions. *Earth-Science  
1220 Reviews*, 145, 117-131, doi:10.1016/j.earscirev.2015.02.007.
- 1221 Rowley, D. B., Forte, A. M., Moucha, R., Mitrovica, J. X., Simmons, N. A., and Grand, S. P.  
1222 (2013). Dynamic topography change of the eastern United States since 3 million years ago.  
1223 *Science*, 340(6140), 1560-1563, doi:10.1126/science.1229180.
- 1224 Rudge, J.F., Champion, M.E.S., White, N., McKenzie, D., and Lovell, B. (2008). A plume  
1225 model of transient diachronous uplift at the Earth's surface. *Earth and Planetary Science  
1226 Letters*, 267(1-2), 146-160, doi:10.1016/j.epsl.2007.11.040.
- 1227 Sahagian, D. (1988). Epeirogenic motions of Africa as inferred from Cretaceous shoreline de-  
1228 posits. *Tectonics*, 7(1), 125-138, doi:10.1029/TC007i001p00125.
- 1229 Salles, T., Flament, N., and Müller, D. (2017). Influence of mantle flow on the drainage of  
1230 eastern Australia since the Jurassic Period. *Geochemistry, Geophysics, Geosystems*, 18(1),  
1231 280-305, doi:10.1002/2016GC006617.
- 1232 Slater, J.G., and Christie, P.A.F. (1980). Continental stretching: An explanation for the post-  
1233 Mid-Cretaceous subsidence of the Central North Sea Basin, *Journal of Geophysical Research:  
1234 Solid Earth*, 85(B7), 3711-3739, doi:10.1029/JB085iB07p03711.

- 1238 Schaeffer, A.J., and Lebedev, S. (2013). Global shear speed structure of the upper mantle and  
 1239 transition zone. *Geophysical Journal International*, 194(1), 417-449, doi:10.1093/gji/ggt095.
- 1240 Schaeffer, A.J. and Lebedev, S. (2014). Imaging the North American continent using wave-  
 1241 form inversion of global and USArray data, *Earth and Planetary Science Letters*, 402, 26-41,  
 1242 doi:10.1016/j.epsl.2014.05.014.
- 1243 Schutt, D. L., and Lesher, C. E. (2006). Effects of melt depletion on the density and seismic ve-  
 1244 locity of garnet and spinel lherzolite. *Journal of Geophysical Research: Solid Earth*, 111(B5),  
 1245 doi:10.1029/2003JB002950.
- 1246 Seton, M., Müller, R.D., Zahirovic, S., Gaina, C., Torsvik, T.H., Shephard, G., Talsma,  
 1247 A., Gurnis, M., Turner, M., Maus, S., and Chandler, M.T. (2012). Global continental  
 1248 and ocean basin reconstructions since 200 Ma. *Earth Science Reviews*, 113, 212–270,  
 1249 doi:10.1016/j.earscirev.2012.03.002.
- 1250 Shephard, G., Müller, R.D. and Seton, M. (2013). The tectonic evolution of the Arctic since  
 1251 Pangea breakup: Integrating constraints from surface geology and geophysics with mantle  
 1252 structure. *Earth Science Reviews*, 124, 148-183, doi:10.1016/j.earscirev.2013.05.012.
- 1253 Shephard, G., Flament, N., Williams, S., Seton, M., Gurnis, M. and Müller, R.D. (2014).  
 1254 Circum-Arctic mantle structure and long-wavelength topography since the Jurassic. *Jour-  
 1255 nal of Geophysical Research: Solid Earth*, 119(10), 7889-7908, doi:10.1002/2014JB011078.
- 1256 Smith, A.G., Smith, D.G., and Funnell, B.M. (1994). *Atlas of Mesozoic and Cenozoic Coastlines*,  
 1257 99 pp., Cambridge University Press.
- 1258 Spasojević, S., and Gurnis, M. (2012). Sea level and vertical motion of continents from  
 1259 dynamic earth models since the Late Cretaceous. *AAPG Bulletin*, 96(11), 2037-2064,  
 1260 doi:10.1306/03261211121.
- 1261 Stephenson, S.N., Roberts, G.G., Hoggard, M.J., and Whittaker, A.C. (2014), A Cenozoic up-  
 1262 lift history of Mexico and its surroundings from longitudinal river profiles. *Geochemistry,*  
 1263 *Geophysics, Geosystems*, 15(12), 4734-4758, doi:10.1002/2014GC005425.
- 1264 Stephenson, S. N., White, N. J., Li, T., and Robinson, L. F. (2019). Disentangling interglacial  
 1265 sea level and global dynamic topography: Analysis of Madagascar. *Earth and Planetary Sci-  
 1266 ence Letters*, 519, 61-69, doi:10.1016/j.epsl.2019.04.029.
- 1267 Stephenson, S., Hoggard, M., and White, N. (2021, April). Global continental residual topogra-  
 1268 phy. In EGU general assembly conference abstracts (pp. EGU21-15505).
- 1269 Valentine, A. P., and D. R. Davies (2020). Global Models From Sparse Data: A Robust Es-  
 1270 timate of Earth's Residual Topography Spectrum. *Geochemistry, Geophysics, Geosystems*,  
 1271 21(8), e2020GC009.240, doi:10.1029/2020GC009240.
- 1272 Van Der Meer, D.G., Spakman, W., Van Hinsbergen, D.J., Amaru, M.L., and Torsvik, T.H.  
 1273 (2010). Towards absolute plate motions constrained by lower-mantle slab remnants, *Nature  
 1274 Geoscience*, 3, 36-40, doi:10.1038/ngeo708.
- 1275 Vilacís, B., Hayek, J. N., Stotz, I. L., Bunge, H.-P., Friedrich, A. M., Carena, S., and Clark,  
 1276 S. (2022). Evidence for active upper mantle flow in the Atlantic and Indo-Australian realms  
 1277 since the Upper Jurassic from hiatus maps and spreading rate changes., *Proc. Roy. Soc. A*,  
 1278 478, 2262, doi:10.1098/rspa.2021.0764.
- 1279 Walker, J.D., Todd, D.B., Ross, A.B., Glazner, A., Farmer, L., and Richard, W. (2006). NAV-  
 1280 DAT: A western North American volcanic and intrusive rock geochemical database, *Special  
 1281 Paper of the Geological Society of America*, 397, doi:10.1130/2006.2397(05).
- 1282 Wang, H., Gurnis, M., & Skogseid, J. (2020). Continent-wide drainage reorganization in North  
 1283 America driven by mantle flow. *Earth and Planetary Science Letters*, 530, 115910. doi:  
 1284 10.1016/j.epsl.2019.115910.
- 1285 Watts, A. B. (2001). Isostasy and Flexure of the Lithosphere. *Cambridge University Press*.
- 1286 Yamauchi, H., and Takei, Y. (2016). Polycrystal anelasticity at near-solidus temperatures. *Jour-  
 1287 nal of Geophysical Research: Solid Earth*, 121(11), 7790-7820, doi:10.1002/2016JB013316.
- 1288 Young, A., Flament, N., Williams, S. E., Merdith, A., Cao, X. and Müller, R. D. (2022). Long-  
 1289 term Phanerozoic sea level change from solid Earth processes, *Earth and Planetary Science  
 1290 Letters*, 584, 117451, doi:10.1016/j.epsl.2022.117451.
- 1291 Ziegler, A., Rowley, D., Lottes, A., Sahagian, D., Hulver, M., and Gierlowski, T. (1985). Paleo-  
 1292 geographic interpretation: with an example from the mid-Cretaceous, *Annual Review of Earth*

1293 and *Planetary Science*, 13, 385-425, doi:10.1146/annurev.earth.13.1.385.